BMC Cancer

RESEARCH

Open Access

# Comprehensive network pharmacology and experimentation to unveil the therapeutic efficacy and mechanisms of gypenoside LI in anaplastic thyroid cancer

Meiyu Liu[1,2], Haidong Liao[3], Qin Peng[4], Junwei Huang[1], Weixiang Liu[1], Mengqiao Dai[5], Zanbing Li[1,5], Yang Xie[1,5], Jiafeng Liu[5], Yong Ying[2*] and Xiangtai Zeng[1,3*]

## Abstract

**Background** Anaplastic thyroid cancer (ATC) is a markedly invasive subtype of thyroid cancer with a poor prognosis. The *Gynostemma pentaphyllum*-derived Gypenoside LI (Gyp LI) can inhibit the growth and metastasis of various tumors. This study was designed to evaluate the pharmacological mechanisms of Gyp LI against ATC via network pharmacology analysis combined with experimental verification.

**Methods** Core targets and signaling pathways were obtained by using the network pharmacological analysis method. Utilizing a combination of in vitro and in vivo methodologies, we conducted a rigorous examination to ascertain the suppressive impact of Gyp LI on the ATC cell lines, specifically 8305 C and C643. Then used western blotting and immunohistochemistry to analyze the inhibitory effects of Gyp LI on SRC kinase and its downstream signaling pathways.

**Results** Through integrative analysis of Gyp LI and ATC-target interactions, 78 candidate targets were identified. Network-based protein-protein interaction (PPI) analysis, combined with molecular docking, pinpointed HSP90AA1, SRC, and CASP3 as pivotal hub genes modulated by Gyp LI. KEGG enrichment analysis further emphasized the PI3K/AKT pathway, highlighting its critical involvement in ATC therapy. Gyp LI significantly inhibits ATC cell proliferation, migration, and invasion while inducing apoptosis, likely via modulation of the SRC/PI3K/AKT axis. Moreover, it enhances iodine uptake in ATC cells by regulating the sodium-iodide symporter pathway.

**Conclusions** Gyp LI effectively inhibits ATC progression by modulating SRC/PI3K/AKT signaling, enhancing apoptosis, and promoting iodine uptake, offering potential therapeutic benefits for ATC treatment.

**Keywords** Gypenoside LI, Anaplastic thyroid cancer, Network pharmacology, SRC/ PI3K/AKT signaling pathway, Iodine uptake

*Correspondence:
Yong Ying
435134372@qq.com
Xiangtai Zeng
xiangtai.zeng@gmu.edu.cn

Full list of author information is available at the end of the article

## Background

Anaplastic thyroid cancer (ATC) is an aggressively invasive malignancy composed of undifferentiated thyroid follicular cells [1, 2]. Early metastasis primarily occurs in the cervical lymph nodes, while in advanced stages, common metastatic sites include the lungs, bones, liver, and other vital organs [3]. The rapid growth rate and aggressive invasiveness of ATC make early diagnosis and treatment particularly challenging. The treatment of ATC currently predominantly relies on surgical intervention [4], radiotherapy [5], and chemotherapy [6]; however, these therapeutic approaches have demonstrated limited efficacy in extending survival [7]. Given the elevated mortality rate linked to ATC and the shortcomings of current therapeutic modalities, there is an imperative to intensify research and advance the development of more efficacious treatment alternatives.

Gynostemma pentaphyllum (GP), vine belonging to the Cucurbitaceae family, is renowned for its distinctive chemical composition and notable medicinal properties [8]. Among its bioactive components, Gypenoside LI (Gyp LI), a tetracyclic triterpenoid saponin of the dammarane type, stands out due to its structural similarity to ginsenosides, contributing to its potential therapeutic value [9]. Previous studies have shown that Gyp exhibits a wide range of biological activities, including antioxidant [10], anti-inflammatory [11], anti-diabetic [12], lipid-lowering, cardiovascular protective, and immunemodulatory [13]. Furthermore, Gyp LI has been proven to significantly inhibit the growth of various cancer cell lines, including A549 lung carcinoma cells [14], renal neoplasms [15], breast cancer cells [16], and melanoma cells [17]. Despite these promising findings, research on the anti-cancer effects of Gyp LI in ATC remains limited.

Network pharmacology, an emerging systems biology approach, has become widely utilized in exploring the complex mechanisms of traditional Chinese medicine (TCM) [18]. Unlike the conventional "one drug, one target" model, network pharmacology emphasizes the interaction between drugs and multiple targets, offering a more comprehensive understanding of the relationships between drugs and diseases, which aids in uncovering multi-target therapeutic mechanisms [19–21]. In this investigation, we utilized network pharmacology, molecular docking, and experimental validation to elucidate the prospective targets and molecular pathways involved in the therapeutic actions of Gyp LI in ATC. Furthermore, we validated these findings in 8305 C cells, C643 cells, and tumor xenograft models. The workflow of our study is shown in Fig. 1.

## Methods

### Network pharmacology analysis

#### *Target prediction of gypenoside LI and ATC*

The molecular formula of Gyp LI was obtained from the PubChem database (https://pubchem.ncbi.nlm.nih.gov) and subsequently used in Swiss Target Prediction (http://swisstargetprediction.ch) to search for the corresponding molecular targets of the drugs and export them in Excel. We searched for the keyword "anaplastic thyroid cancer" to obtain ATC targets from the Therapeutic Target Database (TTD) (http://db.Idrblab.net/ttd), Online Mendelian Inheritance in Man (OMIM) (https://www.omim.org/), and Gene Cards (https://www.genecards.org/). Genes from all three databases were combined. Targets with a score of less than 5 were excluded due to the excessive number of integrated targets. Subsequently, duplicate values were deleted to generate ATC-related targets.

#### *The protein-protein interaction (PPI) and drug-targets-pathway network construction*

To evaluate the interaction between Gyp LI and ATC targets, intersecting targets were obtained using Venny 2.1.0 (https://bioinfogp.cnb.csic.es/tools/venny). The interaction network of the intersecting targets was constructed using the STRING (https://string-db.org/) data base with the parameters "Homo sapiens" and "highest confidence level > 0.4", while setting the rest of the parameters as default. Finally, Cytoscape 3.9.0 software(https://cytoscape.org/), which is an information data analysis and editing software used for designing, constructing, and mapping grids that help identify core targets based on network topology parameters (degrees), was used for visualization.

#### *Gene ontology (GO) and Kyoto encyclopedia of genes and genomes (KEGG) enrichment analyses*

KEGG and GO enrichment analyses were performed using the DAVID database (https://davidbioinformatics.nih.gov/). GO enrichment analysis extracts molecular functions (MF), cell composition (CC), and biological processes (BP) that are closely related to common targets. The GO enrichment results were visualized using bar charts. In this study, relevant signaling pathways were screened at $p < 0.05$. The first 20 related KEGG pathway bubble diagrams were plotted. The KEGG signaling pathway and corresponding target network diagram were constructed using Cytoscape 3.9.0 software.

#### *Molecular docking*

For molecular docking, the mol2 form of Gyp LI (MOL009895) was obtained from TCMSP (https://www.tcmspw.com/tcmsp.php). The three-dimensional str uctures of potential protein targets were retrieved from the Protein Data Bank (PDB) repository (https://www.rc

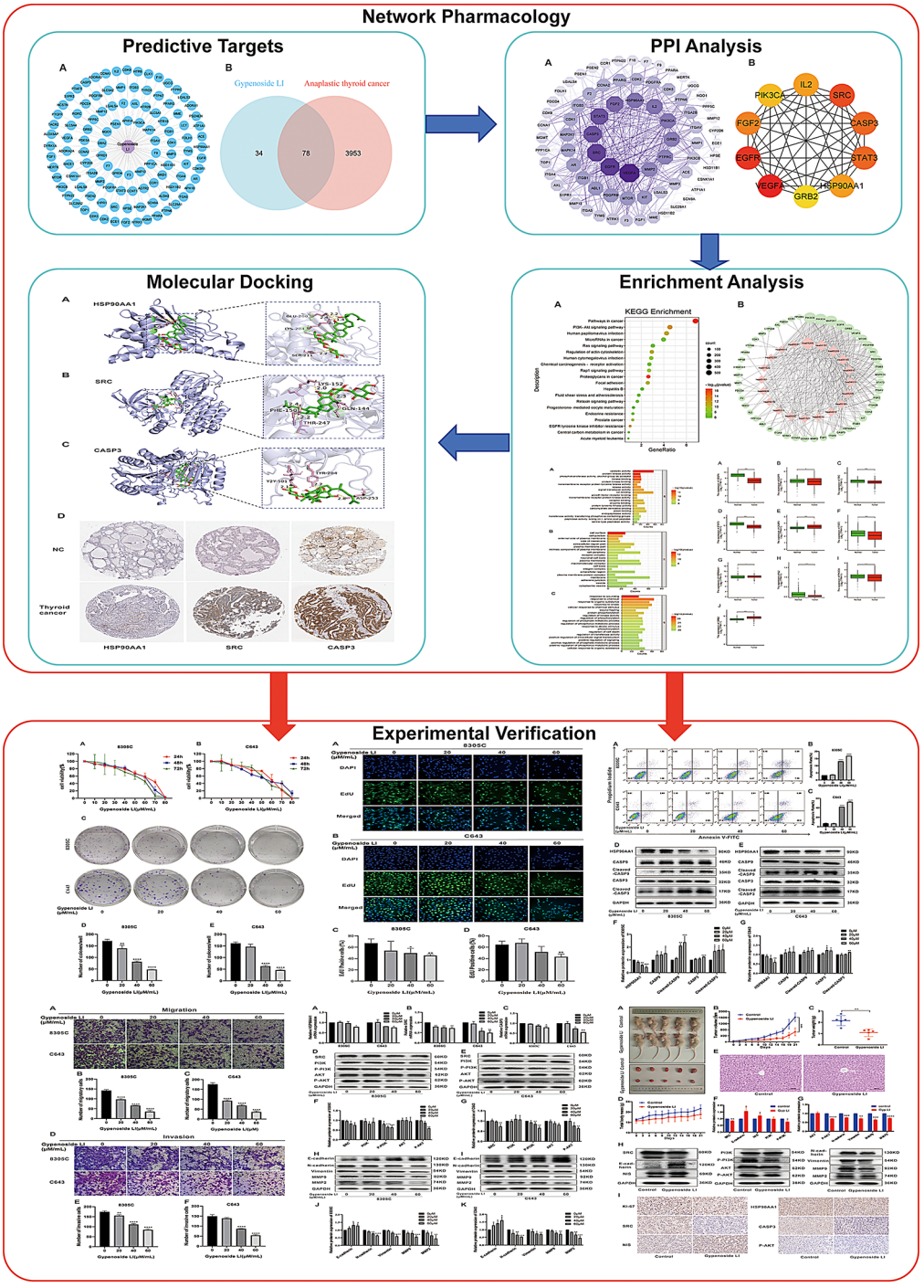


**Fig. 1** Flowchart of this study

sb.org/). Auto dock Vina 1.1.2 was used to dock Gyp LI with the target protein. Blind docking was used because of the inability to accurately determine the core site of the protein. The affinity and score values were used to predict the optimal form of intermolecular docking. Lower scores indicated higher affinity. It is generally believed that when the free energy of docking is lower than −4 Kcal/mol, the binding capacity is stronger. The lowest three docking scores were selected, and the corresponding conformations were visualized using PyMOL 2.5.4. The Human Protein Atlas (https://www.proteinatlas.org/) obtained pathological images of HSP90AA1, SRC, and CASP3 in thyroid tissue and thyroid cancer for analysis.

## Experimental verification in vitro

### Cell lines and cell culture

The ATC cell lines 8305 C and C643 were obtained from Zhejiang Meisen Cell Technology Co., Ltd. The cells were maintained in either Roswell Park Memorial Institute 1640 or Dulbecco's Modified Eagle's Medium, enriched with 10% fetal bovine serum (FBS; Gibco, Grand Island, NY, USA) and penicillin-streptomycin (Gibco), at 37 °C in a humidified incubator containing 5% $CO_2$.

Gypenoside LI (Gyp LI) (CAS No. 94987-10-7; molecular formula: C42H72O14; molecular weight: 801.01 g/mol; purity > 98%) was procured from Chengdu Desite Biotechnology Co., Ltd. To maintain its stability, Gyp LI was solubilized in dimethyl sulfoxide (DMSO) and stored at -20 °C for use in subsequent assays.

### CCK8 assay

The ATC cells were treated with Gyp LI at concentrations of 0, 10, 20, 30, 40, 50, 60, 70, and 80 μM. Respectively, after 24 h, 48 h and 72 h of incubation, the medium was removed, and 100 μL of the new medium mixed with 10% CCK8 solution was pipetted into each well. Following incubation at 37 °C for 1.5 h, the optical density (OD) of the samples was quantified at 450 nm using an enzyme-linked detection system.

### Colony formation assay

ATC cells were plated in six-well plates and cultured for 12 h before being exposed to Gyp LI at concentrations of 0, 20, 40, and 60 μM for 24 h. Subsequently, the cells were reseeded at a density of 1,000 cells per well. The culture medium was replenished every three days, continuing for a total of 12 days. At the conclusion of the culture period, cells were washed with phosphate-buffered saline (PBS), fixed with paraformaldehyde, and subjected to crystal violet staining for assessment. Finally, cells forming colonies were photographed and statistically analyzed.

### 5-Ethynyl-2'-deoxyuridine (EdU) assay

EdU was used to assay cell proliferative capacity. The ATC cells were then treated with different concentrations of Gyp LI for 24 h. Following, the cells were incubated with 2 mL of EdU-labelled medium (10 μM) for 2 h. Subsequently, the fixed and transparent cells were subjected to nuclear staining. Images were captured using a fluorescent microscope.

### Wound healing assay

ATC cells were inoculated into six-well plates at a density of $5 \times 10^5$ cells per well. Upon establishment of a confluent monolayer, a wound was introduced using a micropipette tip. The cells were then exposed to varying concentrations of Gyp LI. Migration of the cells into the wound area was captured at 0 and 24 h using an inverted microscope for analysis.

### Transwell migration and invasion assay

Following treatment with various concentrations of Gyp LI, ATC cells were harvested and resuspended in medium supplemented with 5% FBS. The cells were then seeded into the upper compartment of Transwell inserts, pre-coated either with Matrigel or left uncoated, and placed in the lower chamber containing medium enriched with 20% FBS. After a 24-hour incubation period to facilitate cell migration and invasion, the cells in the lower chamber were fixed with 4% paraformaldehyde and stained with 0.1% crystal violet. Images were captured at 20× magnification using a microscope, and the captured data were subsequently subjected to quantitative analysis and statistical evaluation.

### Flow cytometry

Following treatment with Gyp LI, ATC cells were harvested, washed with chilled PBS, and resuspended in 1× binding buffer. A 100 μL aliquot of the cell suspension was transferred to a flow cytometry tube, combined with 5 μL of Annexin V, and incubated in the dark at an ambient temperature for 5 min. Subsequently, 10 μL of propidium iodide (PI) solution (20 μg/mL) and 400 μL of PBS were added. The samples were promptly analyzed by flow cytometry for further assessment.

### qRT-PCR

Cells were seeded in 6-well plates, treated with Gyp LI for 24 h, and washed twice with pre-cooled PBS. RNA was extracted using an RNA extraction kit (TransGen Biotech). The RNA concentration was measured, and a cDNA synthesis reaction system was prepared. The reaction procedure: incubation at 42 °C for 15 min, 85 °C for 5s, and cooling to 4 °C. The PCR reaction mixture was prepared by incorporating the appropriate forward and reverse primers (Table 1), and the amplification was carried out following the defined reaction protocol. Subsequent data analysis was performed to interpret the results.

### Western blotting

Cell and tissue proteins were extracted and quantified using a BCA protein assay kit (Epizyme Biomedical). Equal quantities of protein were resolved by 10% SDS-PAGE and subsequently transferred onto polyvinylidene fluoride (PVDF) membranes. Prior to antibody incubation, the transfer membrane was subjected to precision excision to exclusively retain the specific molecular weight range encompassing the target proteins. The membranes were blocked and incubated overnight at 4 °C with the corresponding primary antibodies.

**Table 1** qRT-PCR primer sequence

| Gene Name | Forward Primer5-3′ | Reverse Primer5-3′ |
|---|---|---|
| SRC | TTTGGCGAGGTGTGGATG | TGACGATGTAAATGGGCTCC |
| HSP90AA1 | TCTGCCTCTGGTGATGAGATGG | CGTTCCACAAAGGCTGAGTTAGC |
| CASP3 | GGAAGCGAATCAATGGACTCTGG | GCATCGACATCTGTACCAGACC |
| NIS | TGCGGGACTTTGCAGTACATT | TGCAGATAATTCCGGTGGACA |
| TSHR | GGAATGGGGTGTTCGTCTCC | GCGTTGAATATCCTTGCAGGT |
| GAPDH | GGAGCGAGATCCCTCCAAAAT | GGCTGTTGTCATACTTCTCATGG |

After three washes, the membranes were incubated with secondary antibodies at room temperature for 1.5 h. Following incubation, the membranes were exposed to an ECL detection reagent in a darkroom and visualized using a gel imaging system. ImageJ software was employed to analyze the grayscale intensity of each protein band. Quantitative data were processed using appropriate software, and protein band intensities were normalized to GAPDH to account for loading variations.

### Experimental verification in vivo

#### *Nude mouse xenograft model*

All animal experiments were evaluated and approved by the Animal Care and Use Committee of Gannan Medical University (No. LLSC-2024077). Experimental mice were purchased from Jiangsu Huachuang Xinnuo Pharmaceutical Technology Co., Ltd. The 8305 C cells ($5 \times 10^6$) were subcutaneously injected into the left armpit of 10 BALB/c female mice (4 weeks old, 15–18 g). After successful tumor engraftment, the tumors were excised to the size of 10 $mm^3$ and transplanted into the left armpit of the nude mice. The mice were randomly divided into two groups and administered either Gyp LI (gavage, 100 mg/kg) or control solution (gavage, saline + 0.8% DMSO) when the tumor volume reached 50 mm3. Tumor volume and mouse body weight were measured every 2 days. On day 21, the mice were euthanized through cervical dislocation and the tumors were excised and weighed.

#### *Hematoxylin-eosin staining*

Livers of nude mice were fixed with paraformaldehyde, embedded in paraffin, and sectioned. After dewaxing and hydrating, the sections' hematoxylin dye solution was added to the sections and stained for 3–5 min. Following washing with clean water, an eosin dye solution was added to the sections to fully stain them for 1–3 min. After alcohol gradient dehydration, the sections were placed in sealing solution.

#### *Immunohistochemistry*

Tumor tissues from nude mice were fixed in paraformaldehyde, embedded in paraffin, and sectioned. The tissue sections were deparaffinized, followed by rehydration and antigen retrieval. Non-specific binding was blocked by incubating the sections with 5% bovine serum albumin (BSA) for 1 h. Subsequently, the sections were incubated overnight at 4 °C with the appropriate primary antibodies. After thorough washing with buffer, the sections were incubated with species-specific secondary antibodies. Following a subsequent wash, the slides were developed using 3,3'-diaminobenzidine (DAB) substrate. Counterstaining was performed with hematoxylin, and the slides were sealed for microscopic examination.

### Statistical analyses

Statistical analyses were conducted using GraphPad Prism 8.0 (GraphPad Software, Boston, MA, USA) and ImageJ software. Comparisons between two groups were performed using a student's t -test, assuming normal distribution and homogeneity of variances. For comparisons among multiple groups, a one-way analysis of variance (ANOVA) was applied. A significance threshold of $p < 0.05$ was considered statistically significant. All data were derived from at least three independent experiments and are expressed as the mean ± standard deviation (X ± SD). Statistical significance was denoted as follows: $^{*}p < 0.05$, $^{**}p < 0.01$, $^{***}p < 0.001$, and $^{****}p < 0.0001$.

## Results

### Network pharmacology-based analysis

#### *Prediction of Gyp LI and ATC targets*

A total of 112 potential targets for Gyp LI were predicted using the Swiss Target Prediction Database, based on the molecular formula of Gyp LI derived from TCMSP and PubChem (Fig. 2A). Nine ATC targets were identified from the TTD database, while 499 ATC targets were screened using the OMIM database. Additionally, 12,476 ATC targets were retrieved from the GeneCards database, and targets with scores exceeding a predefined threshold of 5 were considered potential candidates for ATC-related activities, yielding a total of 3,674 ATC targets. By integrating all potential targets from the three databases and excluding duplicates, a total of 4,031 distinct ATC targets were obtained. A Venn diagram analysis revealed 78 intersecting genes between the 112 Gyp LI targets and the 4,031 ATC targets (Fig. 2B).

#### *The PPI network of Gyp LI and ATC common targets*

Network construction was conducted to more precisely and intuitively explore the relationships among drugs,

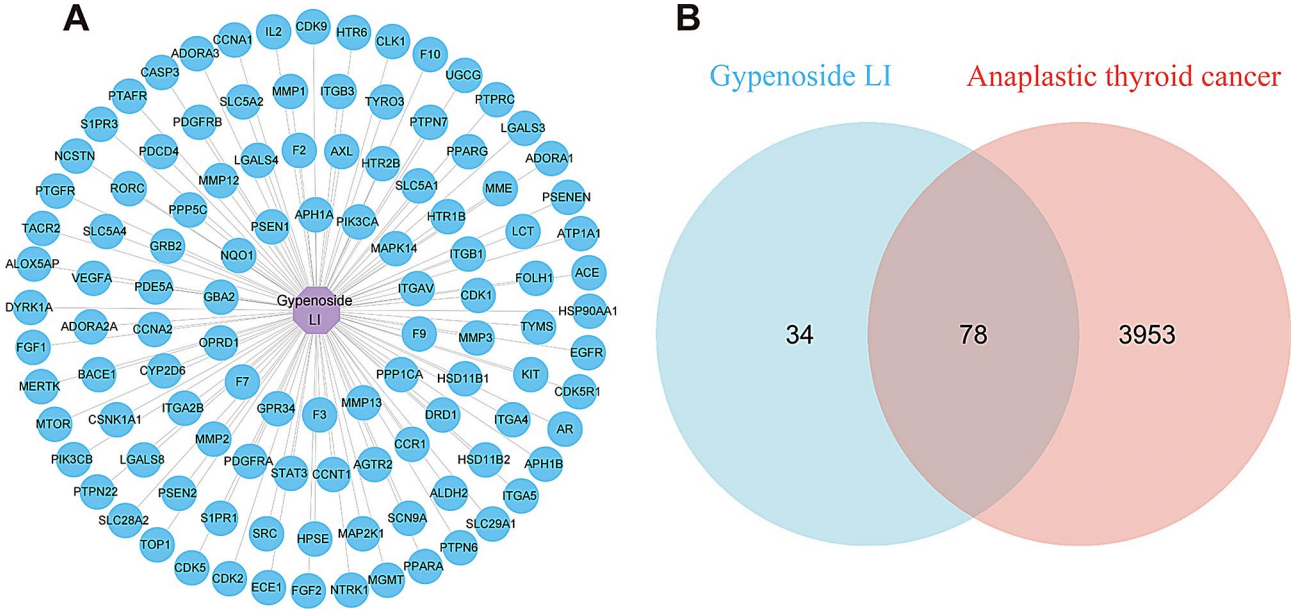


**Fig. 2** Acquisition of potential targets. (**A**). A total of 112 targets were identified, providing insight into the potential molecular interactions of Gyp LI. (**B**). A total of 78 common genes were identified, highlighting potential shared molecular mechanisms between Gyp LI and ATC-related targets

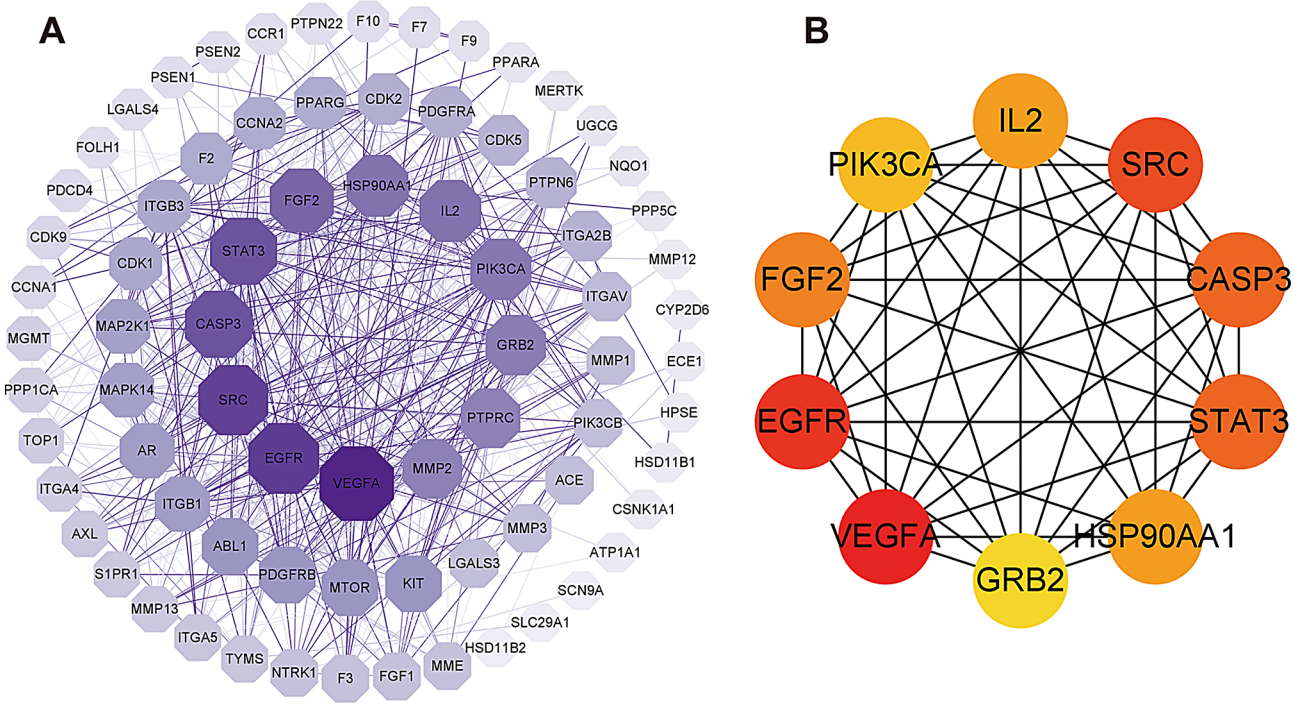


**Fig. 3** Potential hub targets identified via PPI analysis. (**A**). The network, visualized in Cytoscape 3.9.0, consists of 76 nodes representing target proteins and 567 edges denoting interactions between them. (**B**). The hub genes, including VEGFA, EGFR, SRC, STAT3, CASP3, FGF2, HSP90AA1, IL2, PI3KCA, and GRB2, were highlighted, representing key targets with high connectivity and potential roles

targets, and pathways. To this end, the 78 predicted target genes were submitted to the STRING database, where a high-confidence threshold of $>0.4$ was applied for the analysis. The resulting PPI network, visualized using Cytoscape 3.9.0, comprised 76 nodes and 567 edges (Fig. 3A). In this PPI network, the nodes represent the target proteins, while the edges denote the interactions between them; the number of connections for each node, reflected by its degree value, indicates the centrality and significance of the corresponding protein within the network [22]. Subsequently, the CytoHubba plugin was employed to identify the core targets among the potential

candidates, and the top 10 hub genes, namely VEGFA, EGFR, SRC, STAT3, CASP3, FGF2, HSP90AA1, IL2, PI3KCA, and GRB2, were selected based on the degree method (Fig. 3B). Differential analyses of, and survival curve construction for the ten hub genes were performed using TCGA-THCA dataset (S1, S2).

### *GO analysis and KEGG pathway enrichment analysis*

To further investigate the function of Gyp LI in ATC, we executed GO and KEGG enrichment analysis of the 78 overlapping targets. The top 20 enriched GO terms of molecular functions, cellular components, and biological processes are shown in (Fig. 4A-C). Molecular functions include catalytic activity, protein kinase activity, phosphotransferase activity, alcohol group acceptor, etc. The

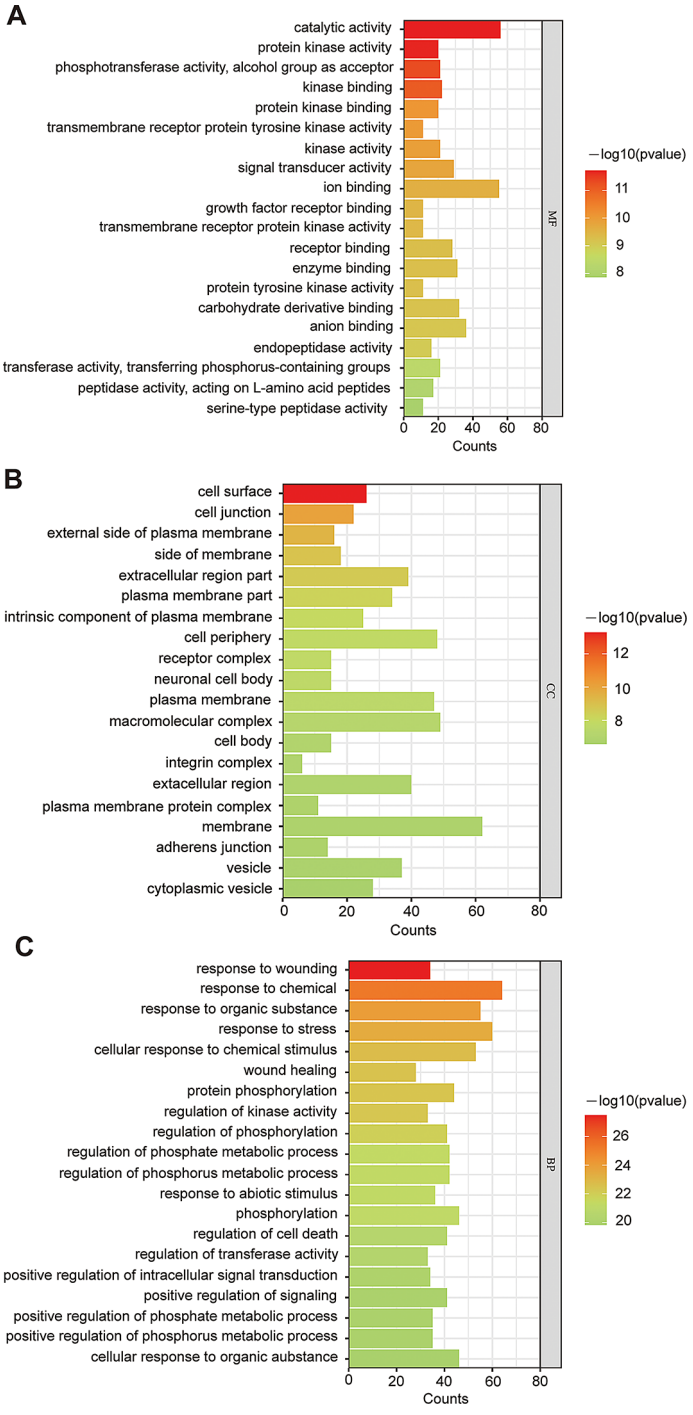


**Fig. 4** Intersection target GO enrichment analysis

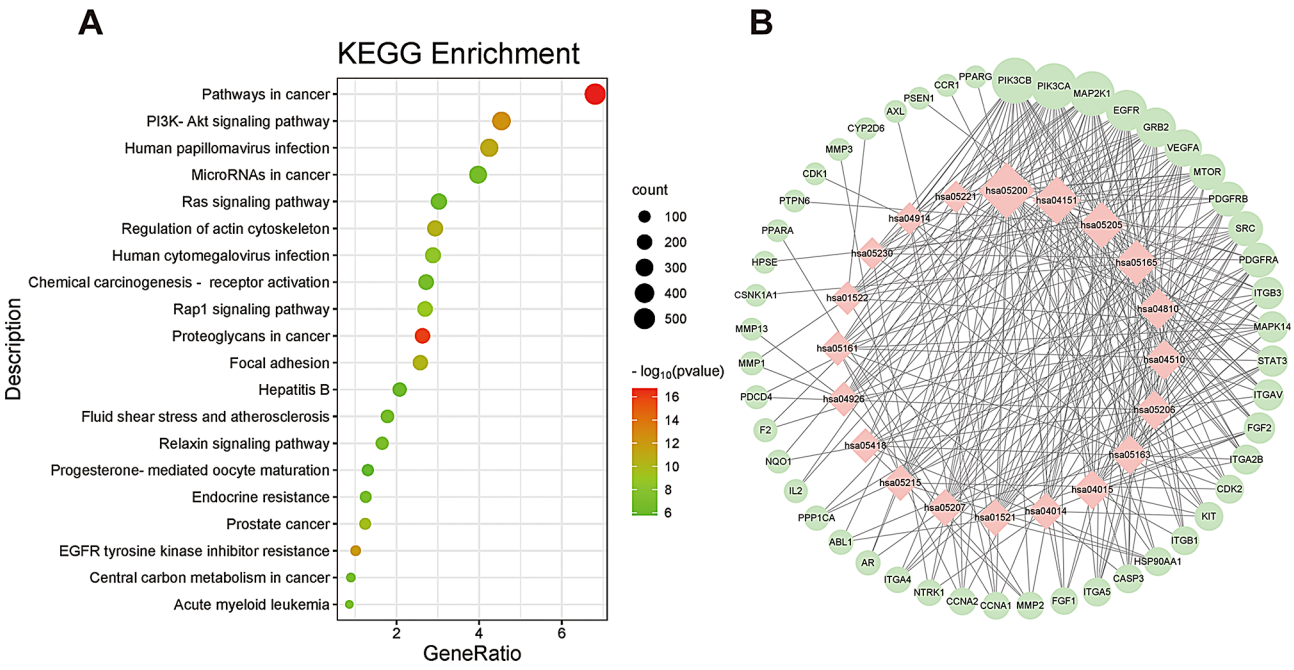


**Fig. 5** (**A**) KEGG enrichment results related to the potential targets of Gyp LI. (**B**) Target-pathway network diagram

cellular components include cell surface, cell junction, external side of plasma membrane, etc. Finally, the biological processes include response to wounding, response to chemical, response to organic substance, among others.

A total of 118 pathways associated with the ATC effects of Gyp LI were identified through KEGG enrichment analysis. Among these, the processes exhibiting the highest number of differentially expressed genes (DEGs) included: pathways in cancer (30 DEGs), the PI3K-AKT signaling pathway (23 DEGs), proteoglycans in cancer (22 DEGs), human papillomavirus infection (21 DEGs), regulation of the actin cytoskeleton (18 DEGs), focal adhesion (16 DEGs), and Ras signaling pathway (13 DEGs) (Fig. 5A). These findings highlight the significant involvement of the PI3K-AKT and Ras signaling pathways in mediating the therapeutic effects of Gyp LI on ATC. Notably, the PI3K-AKT signaling pathway harbored the largest number of DEGs, suggesting its pivotal role in the treatment of ATC. Furthermore, the top 20 enriched KEGG pathways were visualized as a "target pathways" network (Fig. 5B), with the most significantly enriched genes, including PIK3CB, PIK3CA, MAP2K1, EGFR, GRB2, VEGFA, MTOR, PDGFRB, SRC, and PDGFRA. Notably, the KEGG atlas revealed that SRC is positioned upstream of the PI3K/AKT signaling pathway and exerts a direct or indirect regulatory influence on this pathway (S3, S4), further emphasizing its importance in the molecular mechanisms underlying Gyp LI's anti-ATC effects.

**Table 2** Docking and binding energy of gyp LI with ten target molecules

| Component | Gene | PDB ID | ΔGb (Kcal/mol) |
|---|---|---|---|
| Gypenoside LI | HSP90AA1 | 3T0H | -5.84 |
| Gypenoside LI | SRC | 1FMK | -4.87 |
| Gypenoside LI | CASP3 | 6X8I | -3.34 |
| Gypenoside LI | IL2 | 6YIO | -2.88 |
| Gypenoside LI | VEGFA | 1FLT | -2.51 |
| Gypenoside LI | EGFR | 1XKK | -1.81 |
| Gypenoside LI | GRB2 | 1GCQ | -1.55 |
| Gypenoside LI | PI3KCA | 7L1C | -1.38 |
| Gypenoside LI | STAT3 | 6NJS | -0.41 |
| Gypenoside LI | FGF2 | 5X10 | 0.39 |

### *Molecular docking*

Molecular docking, which involves the spatial and energetic alignment of molecules, facilitates the exploration of intermolecular interactions and enables the prediction of binding modes and affinities. The top ten hub targets, identified through the PPI network, were subjected to molecular docking analysis with Gyp LI, with the specific docking scores presented in Table 2. Upon systematic evaluation of the molecular docking outcomes, it was observed that the docking energies of HSP90AA1, SRC, and CASP3 were ranked as the highest, indicating that these targets may exhibit a more significant and direct interaction with Gyp LI. To further elucidate the nature of the interactions between the docking residue sites of Gyp LI and the three targets, PyMOL software was employed, allowing for the visualization of the corresponding protein residues as rod-shaped structures

and the identification of specific interacting residues (Fig. 6A-C). Moreover, data from The Human Protein Atlas revealed that the expression levels of HSP90AA1, SRC, and CASP3 were notably elevated in thyroid cancer tissue when compared to normal thyroid tissue (Fig. 6D), providing additional support for their potential relevance in the context of Gyp LI's therapeutic effects.

## Experimental validation

### *In vitro cytotoxicity of Gyp LI*

To further investigate the inhibitory effect of Gyp LI on the proliferation of ATC cells and to establish the optimal drug concentration for subsequent experiments, a series of CCK-8 assays were conducted using a concentration gradient ranging from 0 to 80 μM (with increments of 10 μM). The CCK-8 results revealed that the half-maximal inhibitory concentrations (IC50) of Gyp LI were 68.46 μM at 24 h, 61.09 μM at 48 h, and 52.97 μM at 72 h for 8305 C cells (Fig. 7A), while for C643 cells, the corresponding IC50 values were 60 μM at 24 h, 57.27 μM at 48 h, and 54.30 μM at 72 h (Fig. 7B). These findings demonstrate that Gyp LI exerts a concentration-dependent inhibition of cell proliferation in both 8305 C and C643 cell lines. Notably, the effects of Gyp LI were most pronounced at 24 h, which was therefore selected as the optimal treatment duration for subsequent investigations. Furthermore, based on the 24-hour IC50 values, four concentrations (0, 20, 40, and 60 μM) were chosen for further experimental evaluation. To further substantiate the proliferative inhibitory potential of Gyp LI on ATC cells, we performed colony formation and EdU assays. The results showed that Gyp LI markedly suppressed the colony-forming ability of both cell lines after 24 h of treatment, with both the number and size of colonies significantly diminished as the drug concentration increased (Fig. 7C-D). Moreover, in comparison to the control group, the number of fluorescently stained cells was significantly reduced in the experimental group, and the morphology of the cells also exhibited noticeable changes (Fig. 8A-D), indicating that Gyp LI effectively inhibits the proliferation of 8305 C and C643 cells in a dose-dependent manner.

### *Gyp LI suppresses ATC cells migration and invasion*

Cell migration and invasion are critical cellular processes, with particular significance in cancer metastasis [23, 24]. This study aimed to investigate the impact of Gyp LI on the migratory and invasive abilities of ATC cell lines. Migration was assessed using both the scratch wound assay and Transwell chamber assay [25]. The results revealed that Gyp LI significantly inhibited cell migration in a dose-dependent fashion. After 24 h of treatment with Gyp LI, the cell migration rate at 0 μM was set as 100%. At concentrations of 20, 40, and 60 μM, the migration of 8305 C cells to the lower chamber was reduced by 31%, 53%, and 74%, respectively. Similarly, the migration of C643 cells was inhibited by 47%, 61%, and 79%, respectively (Fig. 9A-C). These findings were further supported by the results of the wound-healing assay (S5). The scratch assay results demonstrated that the wound healing rates for the control groups of 8305 C and C643 cells were 57.33% and 55.33%, respectively. When treated with Gyp LI at a concentration of 20 μM, the wound healing rates were 54.33% and 47%, respectively, showing no statistically significant difference compared to the control. However, at a Gyp LI concentration of 40 μM, the wound healing rates decreased to 36.31% and 37%, respectively. Further increasing the Gyp LI concentration to 60 μM resulted in wound healing rates of 25% and 23%, respectively. The invasive potential of ATC cells was evaluated using the Transwell chamber assay. Data presented in (Fig. 9D-F) demonstrated that Gyp LI effectively suppressed the invasion of ATC cells in a concentration-dependent manner. When the number of cells invading the lower chamber after 24 h of treatment at 0 μM was set as 100%, the number of 8305 C cells invading the lower chamber after 24 h of treatment with 20, 40, and 60 μM Gyp LI was reduced by 10%, 35%, and 51%, respectively. A similar trend was observed in C643 cells. In conclusion, our findings provide strong evidence that Gyp LI exerts potent inhibitory effects on both the migration and invasion of ATC cells, suggesting its potential as a novel therapeutic approach for metastatic thyroid cancer.

### *Gyp LI inhibited the activation of the SRC/PI3K/Akt signaling pathway*

Network pharmacology analysis revealed the pivotal roles of HSP90AA1, SRC, and CASP3 as key target hubs, as well as the PI3K/AKT signaling pathway in the therapeutic effects of Gyp LI on ATC. To validate these findings, experimental verification was conducted. Firstly, the mRNA expression levels of these core targets were assessed, and the results indicated that Gyp LI treatment significantly downregulated the mRNA expression of HSP90AA1 and SRC, while upregulating the mRNA expression of CASP3 in ATC cells (Fig. 10A-C). Recent studies have demonstrated a close correlation between SRC and cellular invasiveness, as well as a complex regulatory relationship with the PI3K/AKT signaling pathway [26, 27]. To further explore the impact of Gyp LI on this signaling cascade, we examined the expression levels of key proteins involved in the SRC/PI3K/AKT pathway. Notably, with increasing concentrations of Gyp LI, the protein levels of SRC, P-PI3K, and P-AKT in ATC cells progressively decreased (Fig. 10D-G), suggesting that Gyp LI effectively inhibited the activation of the SRC/PI3K/AKT signaling pathway. Given that SRC activation is frequently linked to enhanced cellular invasiveness and

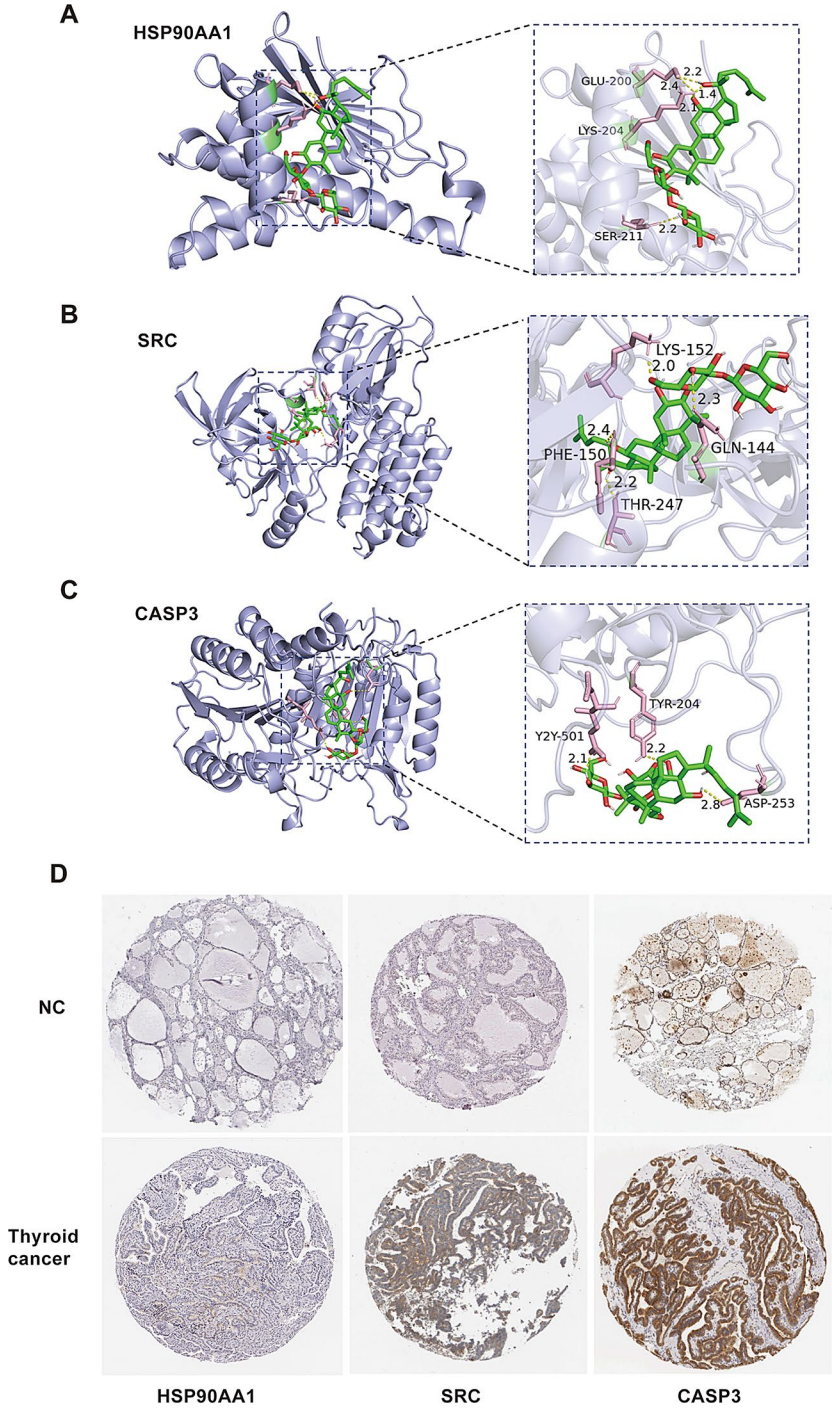


**Fig. 6** Structural Insights into the Molecular Docking of Gyp LI with HSP90AA1, SRC, and CASP3. Molecular docking analyses elucidated the binding configurations, with the green rod structures representing Gyp LI and the pink fan structures delineating the respective binding sites. (**A**) The interaction between HSP90AA1 and Gyp LI was found to involve the residues GLU-200, LYS-204, and SER-211. (**B**) The binding of Gyp LI to SRC was characterized by interactions with the residues GLN-144, PHE-150, LYS-152, and THR-247. (**C**) The residues implicated in the binding of CASP3 to Gyp LI were identified as TYR-204, ASP-253, and TYR-501. (**D**) The immunohistochemical analysis revealed significantly elevated expression levels of HSP90AA1, SRC, and CASP3 in thyroid cancer tissues compared to normal thyroid tissues, suggesting their potential relevance in the pathophysiology of ATC

the emergence of therapeutic resistance in tumor cells, a process that is intimately associated with epithelial-mesenchymal transition (EMT) [28, 29], we proceeded to examine the expression of key EMT markers. The results revealed that Gyp LI treatment led to a significant downregulation of N-cadherin and vimentin, as well as a marked reduction in MMP9 and MMP2 levels, while E-cadherin expression was significantly upregulated

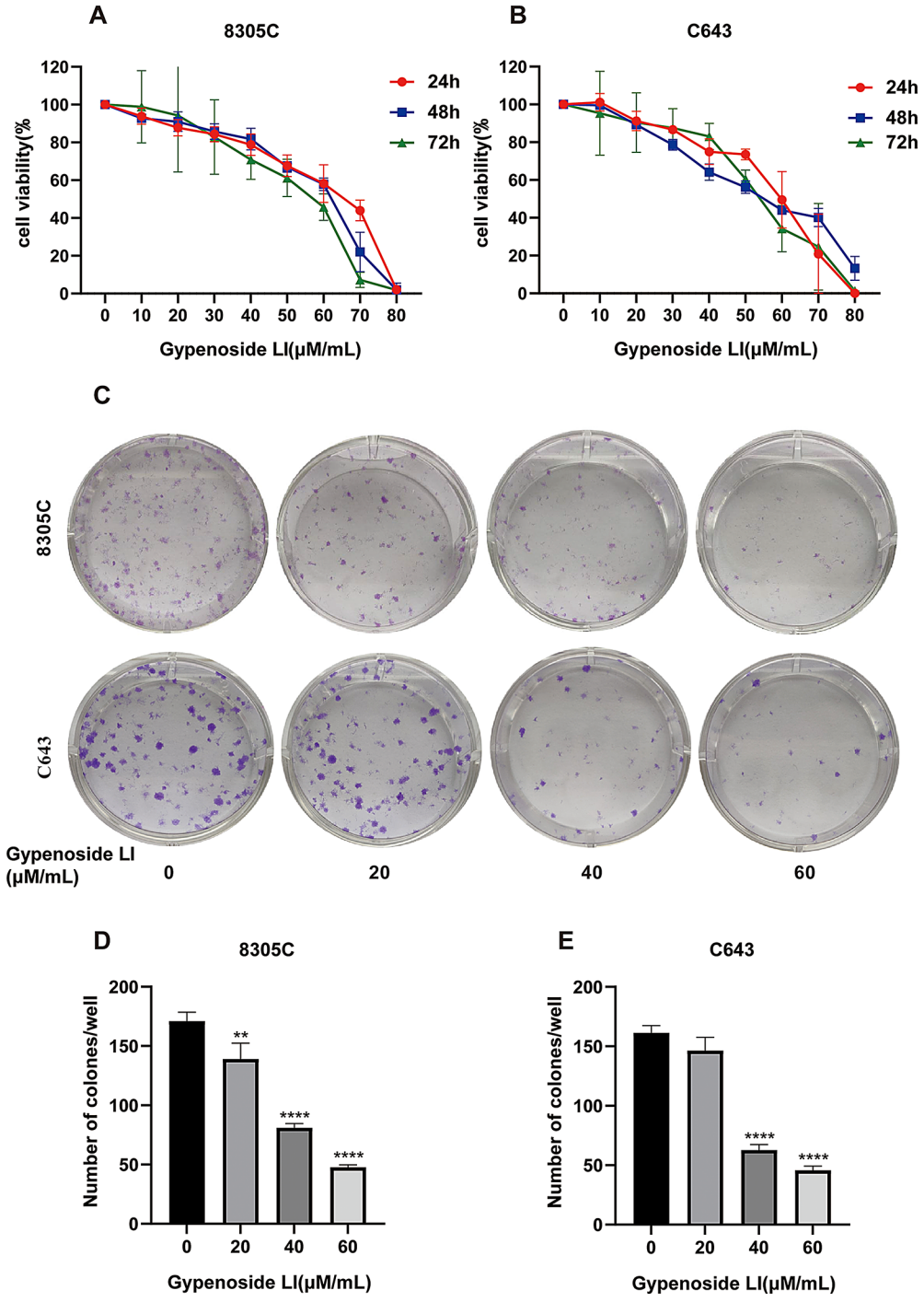


**Fig. 7** Gyp LI inhibited the proliferation of ATC cells. (**A**) Survival rate of 8305 C cells treated with different concentrations of Gyp LI. (**B**) Survival rate of C643 cells treated with different concentrations of Gyp LI. (**C**) The ATC cells treated with Gyp LI formed fewer colonies, as indicated using crystal violet staining. (**D**) Statistical analysis of the colony formation assays. The y-axis indicates the total number of clones in one well

(Fig. 10H-K). In summary, our analysis indicates that Gyp LI inhibits the activation of the SRC/PI3K/AKT signaling pathway, thereby significantly suppressing the migration and invasiveness of ATC cells.

### *Gyp LI induced apoptosis of ATC cells*

Apoptosis is a highly regulated and orderly process of cell death that is initiated by either extrinsic or intrinsic signaling pathways [30]. As a pivotal executioner protein in the apoptotic process, CASP3 plays a crucial role. We suspect that Gyp LI can induce apoptosis in ATC cells,

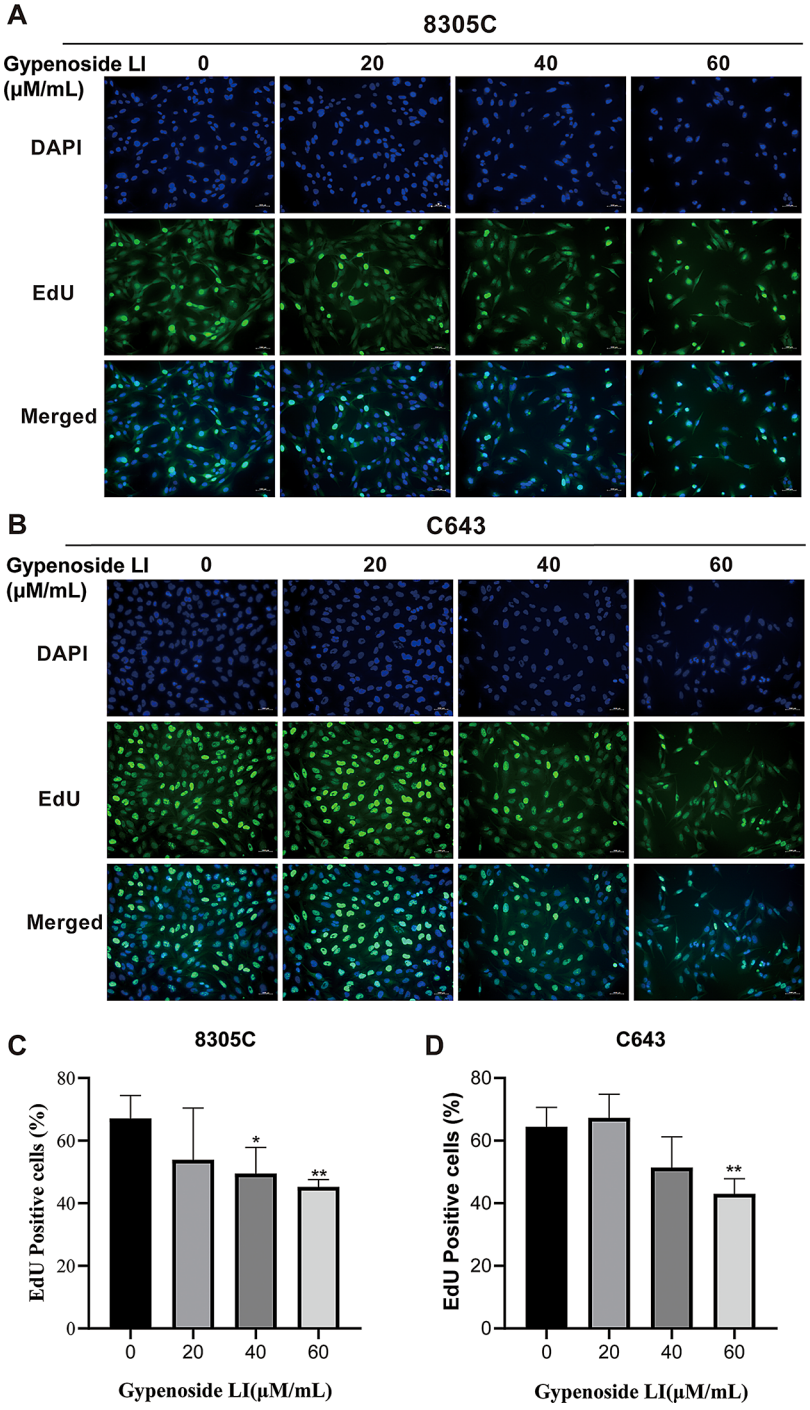


**Fig. 8** Cellular proliferation was evaluated through the EdU incorporation assay. ATC cells were incubated with EdU and counterstained with DAPI to visualize cell nuclei. The proportion of EdU-positive cells was quantified (Magnification: 20×; scale bar = 500 μm)

as our results demonstrate that the mRNA expression of CASP3 increases with the rising concentration of Gyp LI. To further substantiate this hypothesis, we conducted flow cytometry analysis on ATC cell lines 8305 C and C643. The results demonstrated a significant increase in the proportion of both early and late apoptotic cells in the Gyp LI-treated groups compared to the control, with statistical significance (Fig. 11A-C). Additionally, we investigated the modulation of key apoptosis-related proteins. Western blot analysis revealed a marked reduction in HSP90AA1 protein levels following Gyp LI treatment, accompanied by a substantial elevation in the levels of cleaved CASP3 and cleaved CASP9, both of which surpassed the expression levels observed in the control

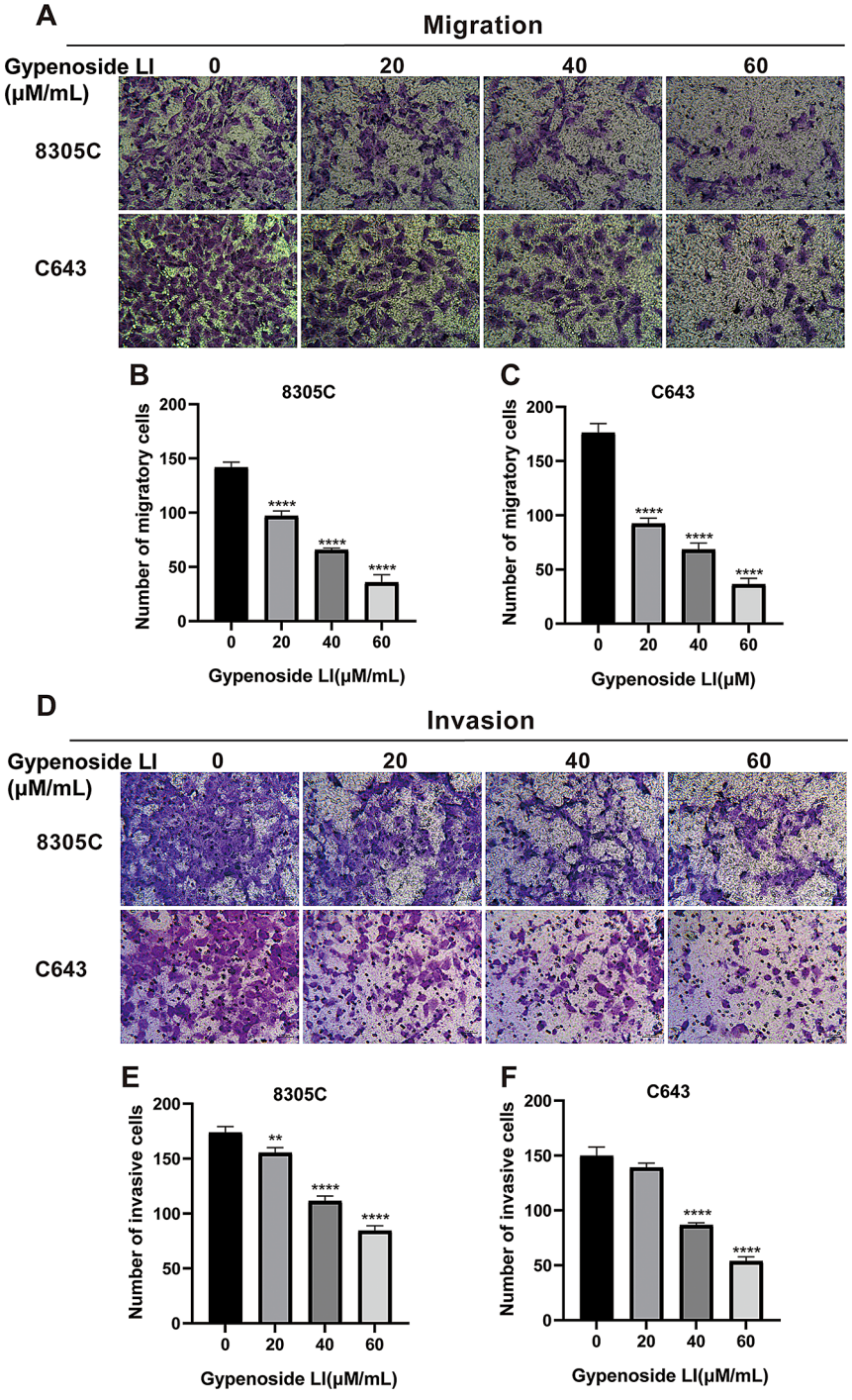


**Fig. 9** Gyp LI inhibits the migration and invasive ability of ATC cells. (**A**-**C**) The Transwell migration assay was used to evaluate the migration capability of ATC cells through the chamber following treatment with Gyp LI. Following treatment with Gyp LI (0, 20, 40, and 60 μM), the mean numbers of 8305 C cells migrating through the chamber were 141.67, 97, 65.67, and 35.67, respectively. Similarly, the mean numbers of C643 cells migrating through the chamber were 176, 92.33, 68.33, and 36.33, respectively. (Magnification: 20×; scale bar = 500 μm). (D-F) The Matrigel Transwell invasion assay was used to evaluate the invasive capability of ATC cells through the basement membrane following treatment with Gyp LI. Following treatment with Gyp LI (0, 20, 40, and 60 μM), the mean numbers of 8305 C cells that migrated through the Matrigel-coated chambers were 173.67, 155.33, 111.33, and 84.33, respectively. Similarly, the mean numbers of C643 cells that migrated through the Matrigel-coated chambers were 149.67, 139, 86.67, and 53.67, respectively. (Magnification: 20×; scale bar = 500 μm)

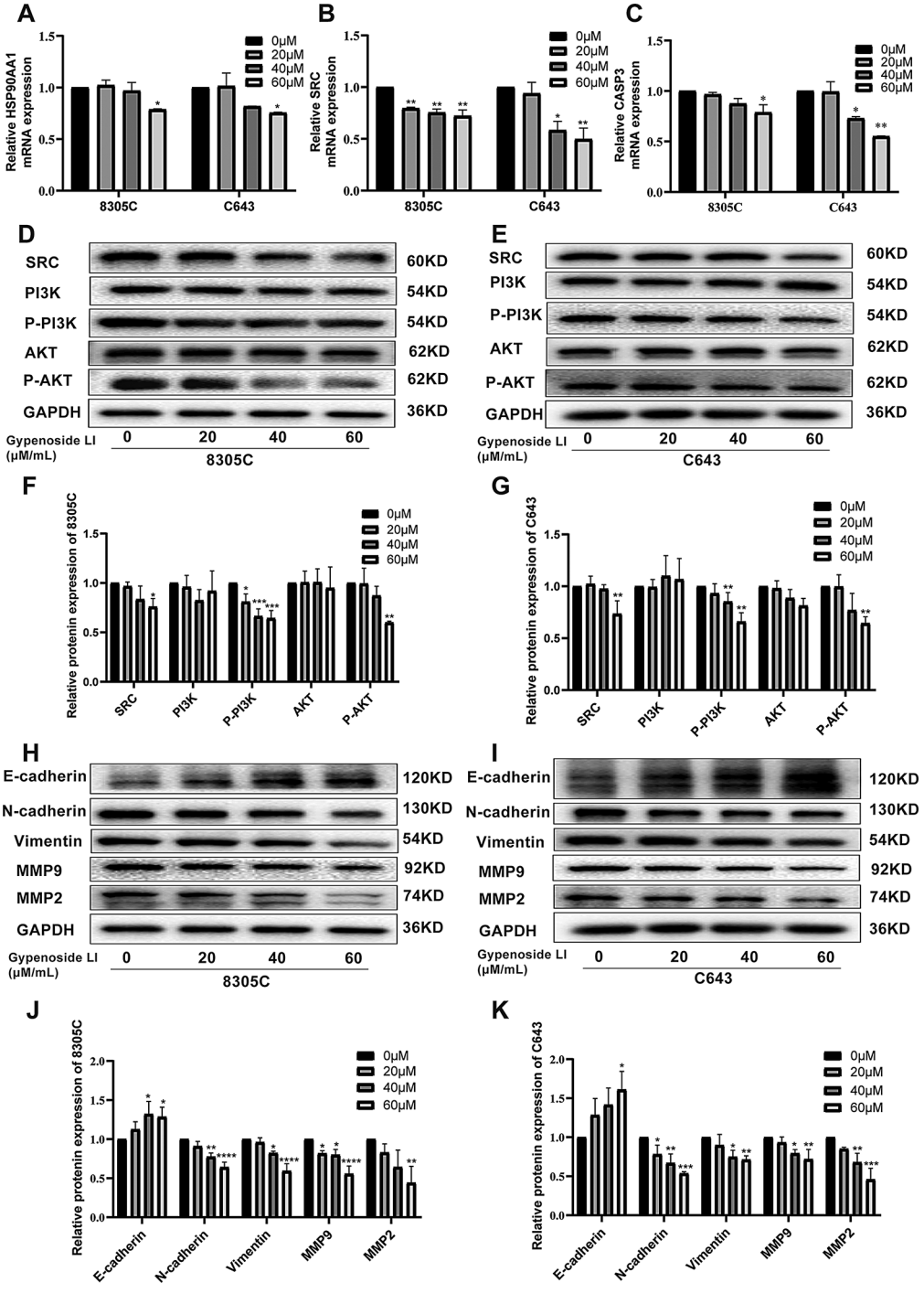


**Fig. 10** Gyp LI Affect the activation of the SRC / PI3K / AKT signaling pathway. (**A**-**C**) HSP90AA1, SRC and CASP3 mRNA expression in ATC cells after Gyp LI treatment. (**D**-**G**) Western blots of ATC cells treated with Gyp LI. The expression of proteins involved in the SRC/PI3K/AKT signaling pathway was monitored in cell lysates. GAPDH was utilized as a loading control for normalization. The Western blot data from three independent experiments were quantitatively analyzed using ImageJ software. Statistical significance was assessed using one-way ANOVA. (**H**-**K**) The Western blot results and corresponding statistical analyses of EMT-related proteins in ATC cells following treatment with Gyp LI

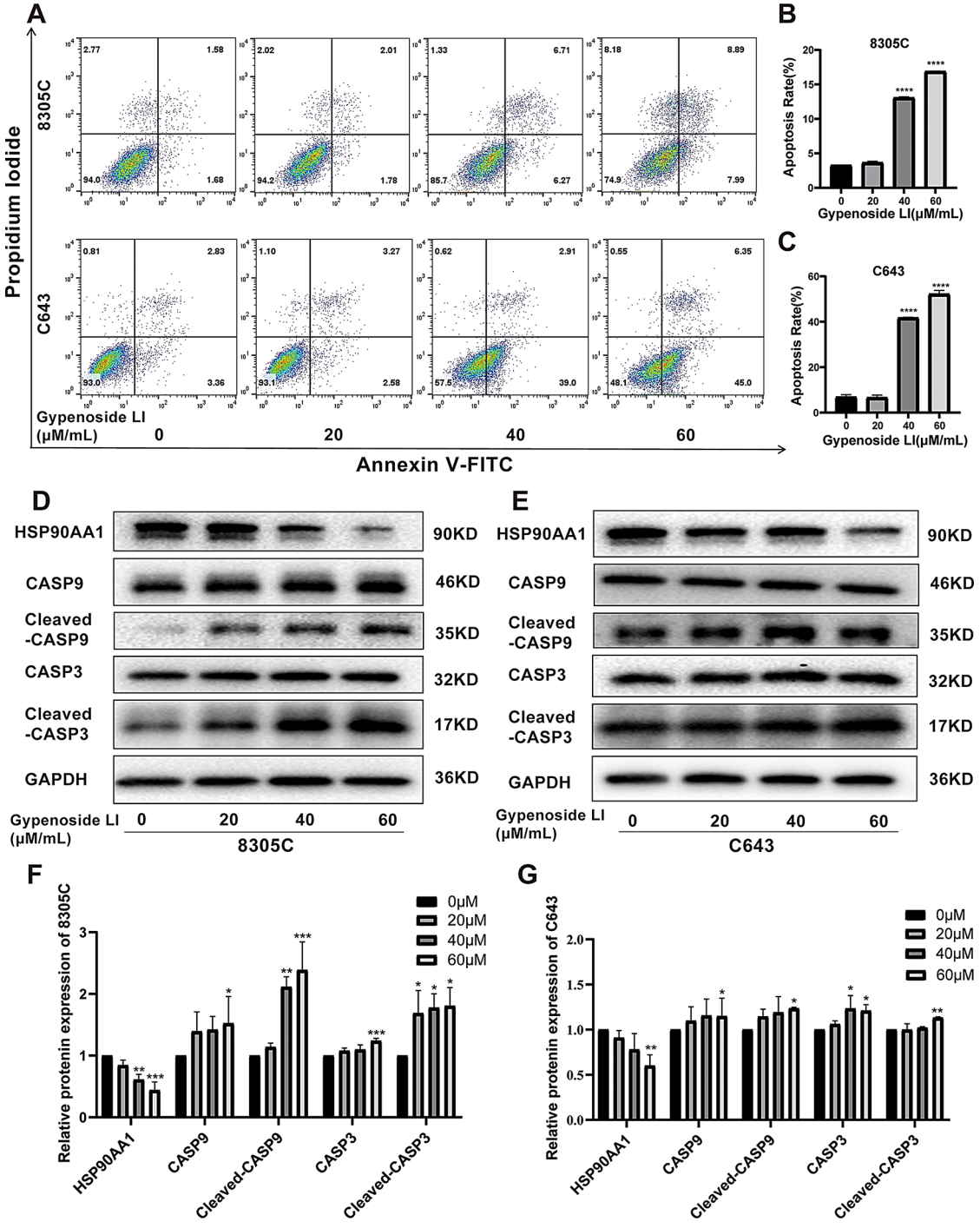


**Fig. 11** Induction of apoptosis in ATC cells by Gyp LI. (**A**-**C**) Flow cytometry analysis showing the distribution of viable, early, and late apoptotic cells in the lower left, lower right and upper right quadrants, respectively. The apoptosis rate was calculated based on the percentage of apoptotic cells. Treatment with 40 and 60 μM Gyp LI significantly enhanced apoptosis in ATC cells. (**D**-**G**) Western blot analysis of ATC cell lysates post-treatment with Gyp LI. The expression levels of HSP90AA1, CASP3, cleaved CASP3, CASP9, and cleaved CASP9 were assessed, with GAPDH used as a loading control

group (Fig. 11D-G). Notably, the elevated presence of cleaved-CASP3, the active form of CASP3, serves as a reliable marker for increased apoptotic activity. Taken together, these data strongly support the conclusion that Gyp LI effectively induces apoptosis in ATC cells, thereby inhibiting tumor cell progression.

### *Gyp LI increases sensitivity of ATC cells to radioactive iodine*

In research related to ATC, the reduction in the expression level of the sodium-iodide symporter (NIS) has been identified as a key factor contributing to tumor dedifferentiation and the decreased ability to uptake iodine [31]. Iodine is an essential component for the synthesis of thyroid hormones, and the proper function of NIS is critical for effective iodine uptake by thyroid cells. Studies have shown that thyroid-stimulating hormone (TSH) binds to its receptor (TSHR), activating the cAMP signaling pathway, which subsequently upregulates the expression of NIS and enhances iodine uptake by thyroid cells [32]. In the present study, we utilized qRT-PCR to measure the mRNA expression levels of TSHR and NIS in ATC cells. The results revealed that the mRNA expression levels of both TSHR and NIS were significantly upregulated in ATC cells treated with Gyp LI (Fig. 12A-B). Moreover, we assessed the changes in NIS protein expression through Western blot analysis, which demonstrated a marked increase in NIS protein expression in Gyp LI-treated ATC cells (Fig. 12C-F). These findings not only confirm the regulatory effect of Gyp LI on NIS expression but also provide strong evidence for the potential of Gyp LI to enhance the sensitivity of ATC cells to radioactive iodine.

### *Gyp LI inhibited tumor formation in nude mice*

To further validate the anti-ATC efficacy of Gyp LI in vivo, we employed a xenograft tumor model for the experiment. The results indicated that, compared to the control group, Gyp LI treatment led to a substantial reduction in tumor volume (Fig. 13A), a marked

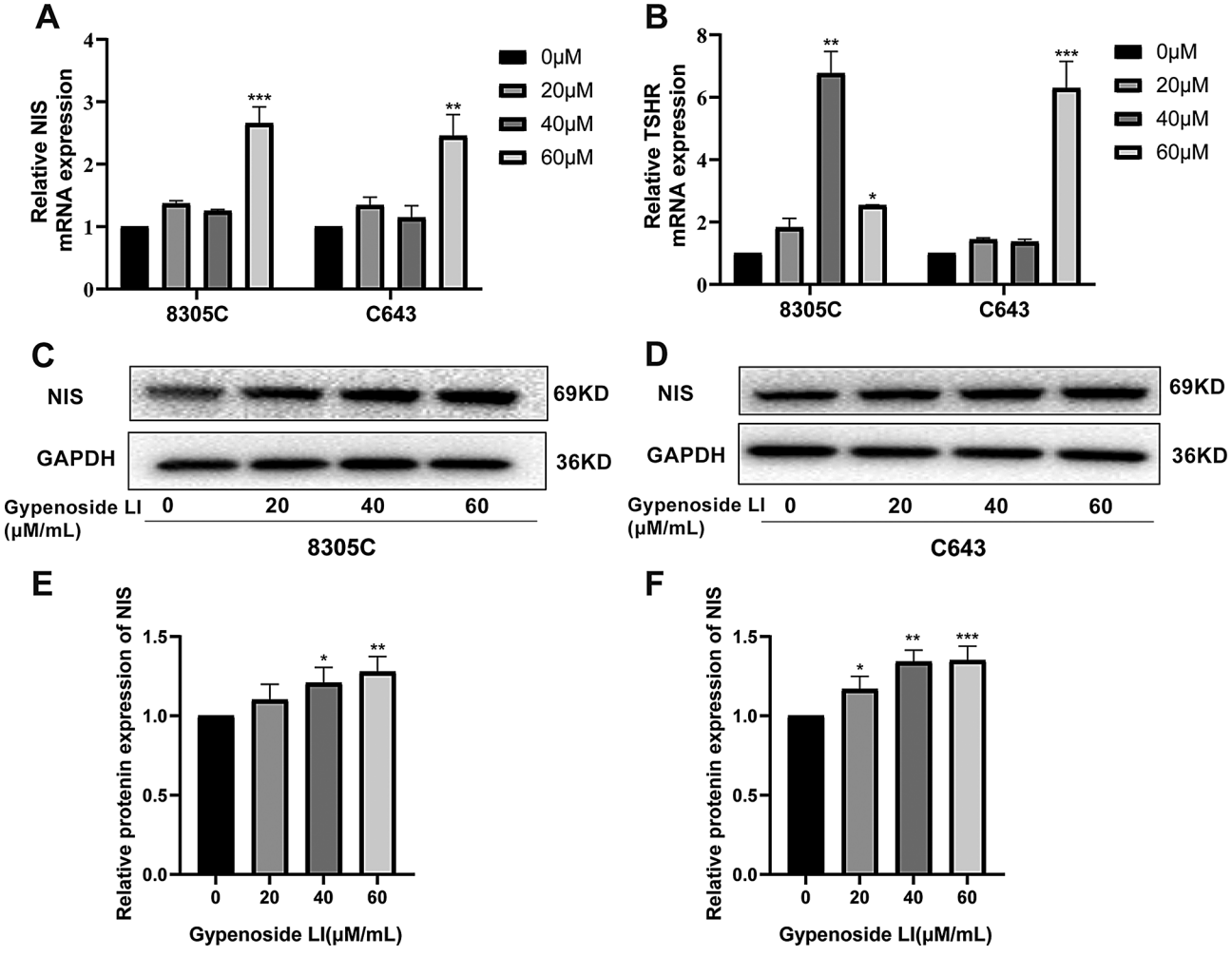


**Fig. 12** Gyp LI enhances the sensitivity of ATC cells to radioactive iodine. (**A**-**B**) Relative mRNA expression levels of TSHR and NIS in 8305 C and C643 cells from the control and Gyp LI-treated groups, as assessed by real-time quantitative PCR. (**C**-**F**) Western blot analysis of 8305 C and C643 cells treated with Gyp LI. Alterations in NIS protein expression were observed in the cell lysates, with GAPDH used as a loading control

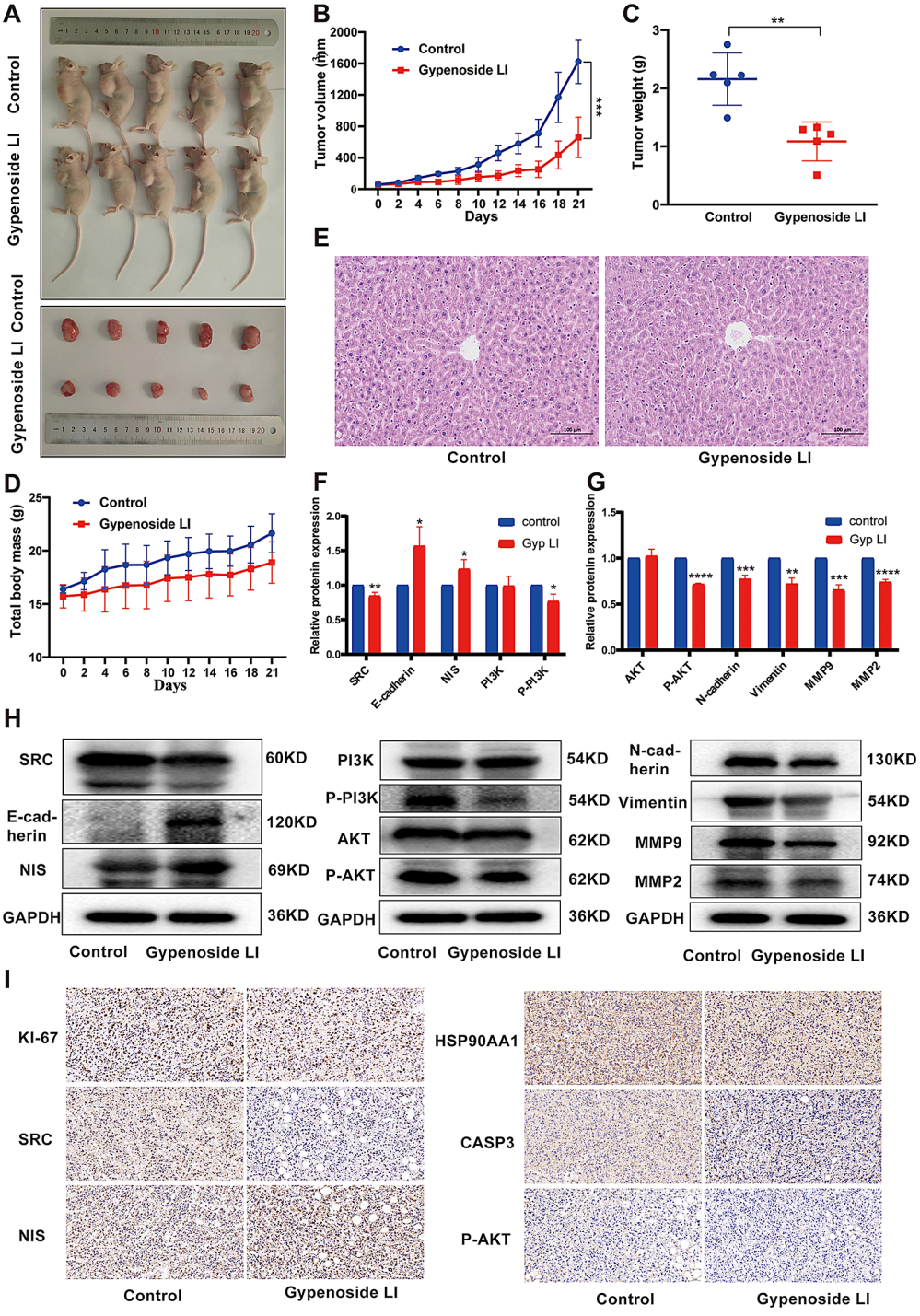


**Fig. 13** Gyp LI inhibits the proliferation of tumors in nude mice. (**A**) Representative images of 8305 C xenograft tumors in mice after treatment with Gyp LI on day 21. (**B**) Tumor growth curves of hormonal nude mice after gavage of Gyp LI at a dose of 100 mg/kg. (**C**) Comparison of tumor volume after stripping on day 21. (**D**) Body weight changes of 8305 C hormonal mice during treatment. (**E**) Histological observation of the tumor tissues after treatment. The liver sections were stained with hematoxylin and eosin, Scale bar, 100 μm. (**F**-**H**) The expression levels of pertinent proteins were assessed in the lysates extracted from tumor tissues, with GAPDH serving as an internal loading control. Quantification of the Western blot outcomes from three separate experiments was conducted employing ImageJ software. Statistical analysis was executed utilizing Student's t-test. (**I**) Examination of protein expression changes within tumor tissues after treatment. Tumor tissue sections were subjected to DAB staining (brown), with hematoxylin counterstaining for nuclei (blue). Scale bar, 50 μm

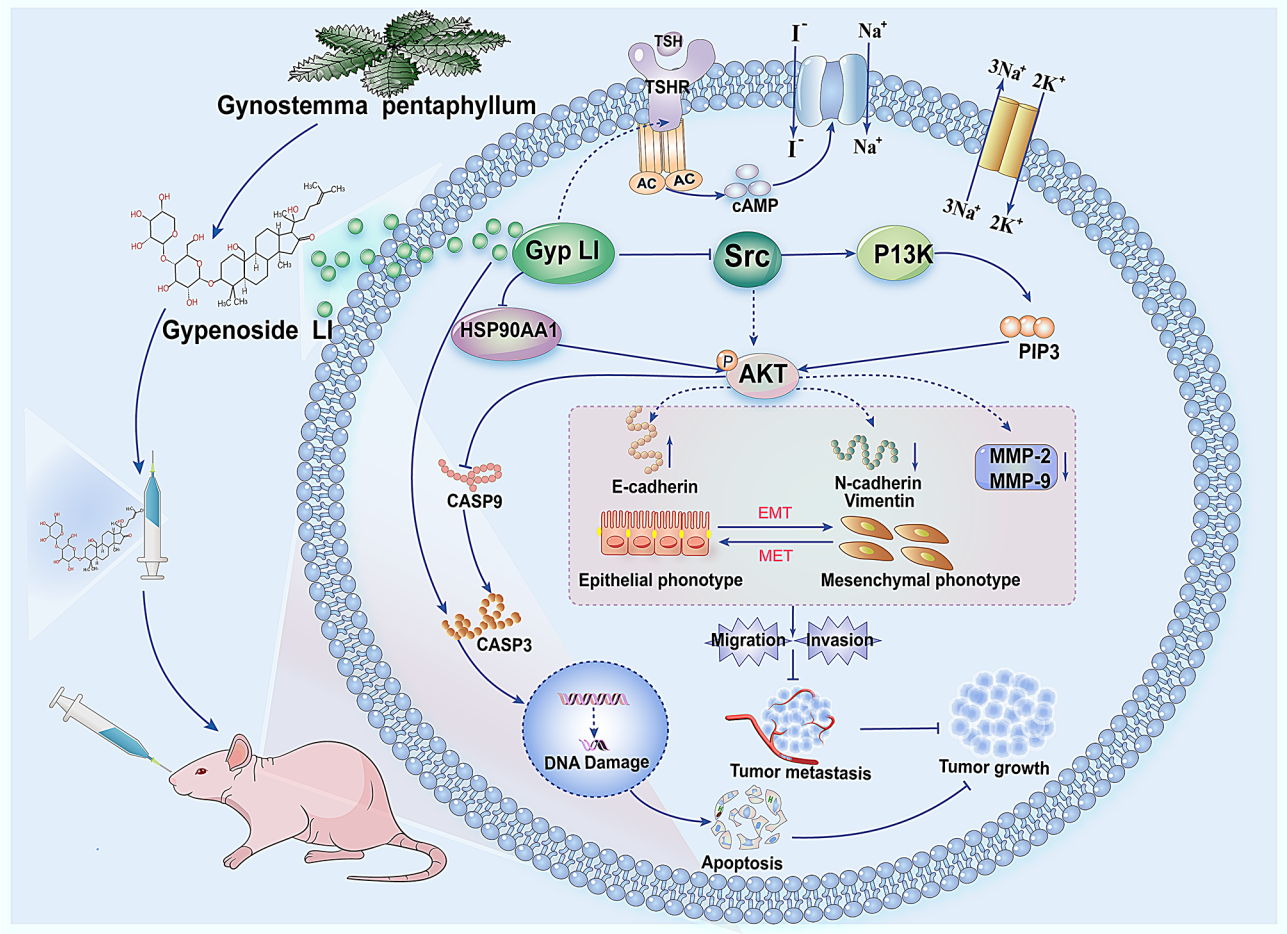


**Fig. 14** Schematic representation of the possible mechanism of inhibition of ATC progression by Gyp LI

deceleration in tumor progression (Fig. 13B), and a significant decrease in tumor mass (Fig. 13C), demonstrating its potent anti-tumor effect. Despite the enhanced tumor growth rate and increased tumor mass observed in the control group, the body weight of the control mice was slightly higher than that of the experimental group (Fig. 13D). Histopathological analysis of liver tissue from tumor-bearing nude mice, using hematoxylin and eosin (HE) staining, revealed no significant histological alterations in liver architecture (Fig. 13E), suggesting that Gyp LI treatment exerts minimal hepatotoxic effects in this model.

In vitro studies have shown that Gyp LI regulates the SRC/PI3K/AKT signaling pathway to suppress EMT in tumor cells. However, it remains uncertain whether Gyp LI exerts a similar regulatory effect in vivo in the nude mouse model. To address this, we performed Western blot and immunohistochemical (IHC) analyses on tumor tissues to evaluate changes in the expression of key proteins. Western blot results revealed that in the tumor tissues of Gyp LI-treated mice, the levels of SRC, P-PI3K, and P-AKT proteins were significantly reduced, while the expression of NIS protein was markedly increased (Fig. 13F-H). Additionally, in EMT-related proteins, while E-cadherin expression was elevated, the expression levels of other EMT markers were significantly decreased (Fig. 13F-H). IHC analysis further showed that the expression of Ki-67, SRC, HSP90AA1, and P-AKT was significantly lower in the Gyp LI group compared to the control group, while the levels of NIS and CASP3 expression were significantly higher (Fig. 13I). Overall, these findings suggest that Gyp LI targets the SRC signaling pathway to inhibit the progression of thyroid tumors in vivo, induces cell apoptosis, and significantly enhances the sensitivity of tumor cells to radioactive iodine (Fig. 14).

## Discussion

ATC is a highly aggressive malignancy with limited treatment options and an extremely poor prognosis. Gyp LI, a saponin compound extracted from Gynostemma pentaphyllum, exhibits a wide range of biological activities, including antioxidant, anti-inflammatory, antitumor, and immunomodulatory effects. Following oral

administration, Gyp LI is primarily absorbed through the gastrointestinal tract; however, its bioavailability is relatively low due to its poor water solubility and high molecular weight. Gyp LI is predominantly metabolized in the liver via the cytochrome P450 (CYP450) enzyme system, undergoing oxidative metabolism. In animal studies, the typical dose range of Gyp LI is 10–100 mg/kg. Research has demonstrated that a dose of 100 mg/kg exhibits significant pharmacological activity in various animal models, with no observable toxic effects reported at this dosage [15].

The core principle of network pharmacology lies in the systematic integration of multidimensional information, including drugs, targets, diseases, and biological pathways, into a complex network structure [33]. In this study, we employed a combination of network pharmacology approaches, molecular docking, and both in vitro and in vivo experimental validation to systematically explore the molecular mechanisms underlying the therapeutic effects of Gyp LI on ATC. By screening public databases, we identified 112 potential targets of Gyp LI, and 4031 targets associated with ATC treatment, and through intersection analysis, we identified 78 candidate targets for Gyp LI in the treatment of ATC. Further PPI analysis revealed the interrelationships among these targets, and degree-based analysis helped us pinpoint 10 key hub targets, suggesting that these targets may play crucial roles in the therapeutic action of Gyp LI against ATC.

KEGG pathway enrichment analysis revealed that Gyp LI intervention in ATC affects 118 signaling pathways ($p$-value $< 0.05$), primarily involving pathways in cancer, the PI3K/Akt signaling pathway, proteoglycans in cancer, human papillomavirus infection, regulation of the actin cytoskeleton, focal adhesion, and Ras signaling pathways. The PI3K/AKT signaling pathway plays a critical role in regulating various cellular processes such as differentiation, metabolism, survival, and apoptosis [34]. However, its aberrant activation often leads to the development of malignancies [35]. The actin cytoskeleton, composed of actin filaments, myosin, and other proteins, plays a crucial role in cell movement, shape maintenance, and cell division [36]. Focal adhesions regulate cell adhesion to the extracellular matrix and mechanical signal transduction, as well as controlling cell growth and differentiation [37]. Based on the analysis of these pathways, we hypothesize that Gyp LI may significantly modulate the motility of ATC cells.

Molecular docking has been widely utilized to discover lead compounds, elucidate binding mechanisms, and guide the optimization of drug molecular structures [38]. To further explore the binding modes and affinities between Gyp LI and potential ATC targets, we performed docking with 10 core targets. Our results indicate that Gyp LI shows low binding energy and high binding capacity with HSP90AA1, SRC, and CASP3 proteins, which is consistent with the findings from the PPI analysis, suggesting that these proteins may serve as potential binding targets for Gyp LI. Overexpression of HSP90AA1 promotes the proliferation, invasion, and drug resistance of thyroid cancer cells and is correlated with the malignancy and poor prognosis of thyroid cancer [39]. Residues GLU-200, LYS-204, and SER-211 may form stable complexes with Gyp LI through hydrogen bonding, electrostatic interactions, or hydrophobic interactions during the molecular binding process, thereby modulating the function of HSP90AA1. SRC, identified as the first oncogene in 1976, plays a key role in tumor growth and progression, with its activity inversely correlating with patient survival [40]. Residues GLN-144, PHE-150, LYS-152, and THR-247 may interact with Gyp LI through similar non-covalent interactions, such as hydrogen bonding, electrostatic forces, or hydrophobic effects, thereby modulating the activity of SRC kinase. CASP3 is a key executor in the apoptosis signaling pathway and plays key roles in regulating the growth and homeostatic maintenance of both normal and malignant cells [41]. We confirmed the expression of these three core genes in ATC through public databases, although some findings remain unverified due to limitations in sample size and database resources. Further studies are needed to elucidate the roles of these genes in ATC and the impact of Gyp LI on them.

In vitro and in vivo experiments were conducted to validate the results of the network pharmacology analysis and to clarify the mechanisms by which Gyp LI treats ATC. Using CCK-8, colony formation, and EdU assays, we observed that Gyp LI inhibits ATC cell proliferation in a dose-dependent manner. Cell apoptosis is a protective mechanism against cancer progression and plays a key role in anticancer therapy [42]. Our study demonstrated that Gyp LI significantly increased the mRNA level of Caspase-3 and the protein level of cleaved Caspase-3 in ATC cells, and flow cytometry analysis confirmed that Gyp LI effectively induced apoptosis. These results suggest that Gyp LI promotes apoptosis in ATC cells. Furthermore, Gyp LI not only inhibits ATC cell migration and invasion but also enhances the sensitivity of ATC cells to radioactive iodine.

Focusing on the PI3K/AKT signaling pathway, which corresponds to a large number of targets, studies found that excessive activation of the PI3K-AKT signaling pathway promotes cell proliferation and migration while inhibiting apoptosis [43–45]. Studies have shown that SRC can activate the PI3K/AKT pathway by directly phosphorylating the p85 subunit of PI3K [46], while also indirectly regulating the phosphorylation state of AKT through other downstream effector molecules, thereby further amplifying the signaling transduction of this

pathway [47]. HSP90AA1 promotes tumor cell proliferation and invasion by stabilizing various pro-proliferative proteins, such as AKT and ERK [48], and inhibits tumor cell apoptosis by stabilizing anti-apoptotic proteins [49]. We found that Gyp LI significantly reduced the mRNA levels of SRC and decreased the protein expression of SRC, p-PI3K, and p-AKT, suggesting that Gyp LI may inhibit cell proliferation, invasion, and promote apoptosis by suppressing the SRC/PI3K/AKT pathway. In vivo results further support this conclusion. Increased endogenous NIS expression is associated with inhibition of the PI3K/Akt and MAPK signaling pathways [50]. In this study, Gyp LI was identified as a promising compound capable of significantly enhancing the endogenous expression of NIS, thereby restoring the affinity of radioactive iodine in ATC.

There have been studies reporting the combination of tyrosine kinase inhibitors and HSP90 inhibitors [51]. Studies have demonstrated that the Hsp90 inhibitor NVP-AUY922 enhances the radiosensitivity of lung cancer cell lines with acquired resistance to EGFR-tyrosine kinase inhibitors [52]. Combination therapy with the HSP90 inhibitor AUY922 and the tyrosine kinase inhibitor erlotinib is associated with drug-related adverse events, including diarrhea, rash, hyperglycemia, and night blindness [53]. Gyp LI, by simultaneously inhibiting SRC and HSP90AA1, may more effectively block key signaling pathways in tumor cells, thereby reducing the occurrence of drug resistance. In contrast, as a single-molecule dual-target inhibitor, Gyp LI may achieve a better balance between efficacy and safety. Future research could focus on structural biology studies to elucidate the binding modes of Gyp LI with its target molecules and further analyze how this dual-targeting mechanism synergistically inhibits critical signaling pathways in tumor cells, providing a theoretical foundation for drug optimization.

Overall, our findings demonstrate that Gyp LI exerts significant inhibitory effects on ATC in the 8305 C and C643 cell lines, as well as in tumor xenograft models, which may be closely linked to its suppression of the SRC/PI3K/AKT signaling pathway. However, the mechanism underlying Gyp LI's anti-ATC effects remains multifaceted, involving various pharmacological actions. While we have identified several key targets and associated signaling pathways, further pharmacological investigations are needed to provide a more comprehensive understanding of these complex mechanisms. Nonetheless, these findings offer strong pharmacological support for the potential use of Gyp LI in the treatment of ATC and lay a solid foundation for the development of Gyp LI as a novel therapeutic strategy for this aggressive cancer. Due to limitations in experimental conditions, the long-term effects of Gyp LI have not been thoroughly investigated. Future studies should include clinical trials to evaluate the long-term efficacy and safety of Gyp LI. Additionally, incorporating xenograft models using the C643 cell line and expanding the dose range (e.g., including very low and very high dose groups) would provide a more comprehensive assessment of the dose-response relationship. Currently, data on the in vivo toxicity of Gyp LI are limited. Further research is needed to determine its maximum tolerated dose (MTD) and pharmacokinetic profile, which will aid in optimizing in vivo dosing strategies.

## Conclusion

Gyp LI significantly inhibits tumor proliferation and invasion, while promoting apoptosis in ATC cell lines (8305 C and C643) and tumor xenograft models, likely through the suppression of the SRC/PI3K/AKT signaling pathway. Moreover, Gyp LI notably enhances the endogenous expression of NIS, thereby restoring the affinity for radioactive iodine, offering promising potential for ATC treatment.

## Supplementary Information

The online version contains supplementary material available at https://doi.org/10.1186/s12885-025-14231-8.

Supplementary Material 1

Supplementary Material 2

Supplementary Material 3

Supplementary Material 4

Supplementary Material 5

### Author contributions

Meiyu Liu：Validation、Writing – original draft、Data curation. Haidong Liao：Validation. Qin Peng: Validation. Junwei Huang: Visualization. Weixiang Liu: Visualization. Mengqiao Dai: Validation. Zanbing Li: Validation. Yang Xie: Funding acquisition、Methodology. Jiafeng Liu: Supervision. Yong Ying: Funding acquisition. Xiangtai Zeng: Funding acquisition、Writing – review. All authors reviewed the manuscript.

### Funding

This work (including the open-access publication fees) was financially supported by the National Natural Science Foundation of China (No.82460498); Project of Science and Technology Program of Jiangxi Province Chinese Medicine for 2023 (No.2023B0202) and Ganzhou Key Laboratory of Thyroid Tumors (No.20220101-24).

### Data availability

The necessary data that support the findings of this study are available as open data via the online data repository: The PubChem database (https://pubchem.ncbi.nlm.nih.gov); Swiss TargetPrediction (http://swisstargetprediction.ch/); TTD (http://db.idrblab.net/ttd); OMIM (https://www.omim.org/); Gene Cards (https://www.genecards.org/); The Human Protein Atlas (https://www.proteinatlas.org/); The Protein Data Bank database (https://www.rcsb.org/); DAVID database (https://davidbioinformatics.nih.gov/). The datasets during and/or analysed during the current study available from the corresponding author on reasonable request.

## Declarations

**Ethics approval and consent to participate**
All animal experiments were evaluated and approved by the Animal Care and Use Committee of Gannan Medical University (No. LLSC-2024077).

**Competing interests**
The authors declare no competing interests.

**Author details**
[1]Department of Thyroid and Hernia Surgery, First Affiliated Hospital of Gannan Medical University, Ganzhou, Jiangxi 341000, China
[2]Ganzhou Key Laboratory of Thyroid Cancer, Ganzhou, Jiangxi 341000, China
[3]Department of General Surgery, First People's Hospital of Longnan, Longnan, Jiangxi 341706, China
[4]Department of Pathology, First Affiliated Hospital of Gannan Medical University, Ganzhou, Jiangxi 341000, China
[5]Institute of Thyroid Diseases of Gannan Medical University, Ganzhou, Jiangxi 341000, China

Received: 9 January 2025 / Accepted: 28 April 2025
Published online: 14 May 2025

**References**

1. Boucai L, Zafereo M, Cabanillas ME. Thyroid Cancer: Review[J] JAMA. 2024;331(5):425–35.
2. Bray F, Laversanne M, Sung H. Global cancer statistics 2022: GLOBOCAN estimates of incidence and mortality worldwide for 36 cancers in 185 countries[J]. Cancer J Clin. 2024;74(3):229–63.
3. Qian C, Jiang L, Xu S. Advances in targeted therapy for anaplastic thyroid carcinoma[J]. Zhejiang Da Xue Xue Bao Yi Xue Ban = J Zhejiang Univ Med Sci. 2021;50(6):685–93.
4. Aras A, Karayil AR. Optimal surgical approaches for thyroid cancer: A comparative analysis of efficacy and Complications[J]. Med Sci Monitor: Int Med J Experimental Clin Res. 2024;30:e942619.
5. Bible KC, Kebebew E, Brierley J. 2021 American thyroid association guidelines for management of patients with anaplastic thyroid Cancer[J]. Thyroid: Official J Am Thyroid Association. 2021;31(3):337–86.
6. Dickerson K, Milas M, Metzger R. Neoadjuvant systemic therapy for inoperable differentiated thyroid cancers: impact on tumor resectability[J]. Surgery. 2025;177:108836.
7. Rao SN, Smallridge RC. Anaplastic thyroid cancer: An update[J]. Best Practice & Research. Clinical Endocrinology & Metabolism, 2023, 37(1): 101678.
8. Nguyen NH, Ha TKQ, Yang JL. Triterpenoids from the genus gynostemma: chemistry and Pharmacological activities[J]. J Ethnopharmacol. 2021;268:113574.
9. Li Y, Lin W, Huang J. Anti-cancer effects of gynostemma pentaphyllum (Thunb.) Makino (Jiaogulan)[J]. Chin Med. 2016;11:43.
10. Liang HZ, Lu PX, Chu LL. Dammarane-type saponins from gynostemma pentaphyllum and their anti-aging activities via up-regulating mitochondria related proteins[J]. Phytochemistry. 2023;213:113744.
11. Yue SR, Tan YY, Zhang L. Gynostemma pentaphyllum polysaccharides ameliorate non-alcoholic steatohepatitis in mice associated with gut microbiota and the TLR2/NLRP3 pathway[J]. Front Endocrinol. 2022;13:885039.
12. Wang Z, Wang Z, Huang W. Antioxidant and anti-inflammatory activities of an anti-diabetic polysaccharide extracted from gynostemma pentaphyllum herb[J]. Int J Biol Macromol. 2020;145:484–91.
13. Xiao MY, Pei WJ, Li S. Gypenoside L inhibits hepatocellular carcinoma by targeting the SREBP2-HMGCS1 axis and enhancing immune response[J]. Bioorg Chem. 2024;150:107539.
14. Xing SF, Liu LH, Zu ML. The inhibitory effect of gypenoside stereoisomers, gypenoside L and gypenoside LI, isolated from gynostemma pentaphyllum on the growth of human lung cancer A549 cells[J]. J Ethnopharmacol. 2018;219:161–72.
15. Liu H, Li X, Xie J. Gypenoside L and gypenoside LI inhibit proliferation in renal cell carcinoma via regulation of the MAPK and arachidonic acid metabolism Pathways[J]. Front Pharmacol. 2022;13:820639.
16. Zu ML, Duan Y, Xie JB. Gypenoside LI arrests the cell cycle of breast cancer in G0/G1 phase by down-regulating E2F1[J]. J Ethnopharmacol. 2021;273:114017.
17. Zu ML, Piao XL, Gao JM. Monomer gypenoside LI from gynostemma pentaphyllum inhibits cell proliferation and upregulates expression of miR-128-3p in melanoma cells[J]. J Biochem Mol Toxicol. 2020;34(5):e22460.
18. Zhang P, Zhang D, Zhou W. Network pharmacology: towards the artificial intelligence-based precision traditional Chinese medicine[J]. Brief Bioinform. 2023;25(1):bbad518.
19. Liu JX, Zhang X, Huang YQ. Multi-level bioinformatics resources support drug target discovery of protein-protein interactions[J]. Drug Discovery Today. 2024;29(5):103979.
20. Zhao L, Zhang H, Li N. Network Pharmacology, a promising approach to reveal the Pharmacology mechanism of Chinese medicine formula[J]. J Ethnopharmacol. 2023;309:116306.
21. Wang K, Qian R, Li H. Interpreting the Pharmacological mechanisms of Shosaiko-to on thyroid carcinoma through combining network Pharmacology and experimental Evaluation[J]. ACS Omega. 2022;7(13):11166–76.
22. Li Y, Ilie L. SPRINT: ultrafast protein-protein interaction prediction of the entire human interactome[J]. BMC Bioinformatics. 2017;18(1):485.
23. Cambria E, Coughlin MF, Floryan MA. Linking cell mechanical memory and cancer metastasis[J]. Nat Rev Cancer. 2024;24(3):216–28.
24. Chastney MR, Kaivola J, Leppänen VM. et.al. The role and regulation of integrins in cell migration and invasion[J]. Nat Rev Mol Cell Biol, 2024.
25. Bouchalova P, Bouchal P. Current methods for studying metastatic potential of tumor cells[J]. Cancer Cell Int. 2022;22(1):394.
26. Roskoski R. Src protein-tyrosine kinase structure, mechanism, and small molecule inhibitors[J]. Pharmacol Res. 2015;94:9–25.
27. Xu R, Song J, Ruze R. SQLE promotes pancreatic cancer growth by attenuating ER stress and activating lipid rafts-regulated Src/PI3K/Akt signaling pathway[J]. Cell Death Dis. 2023;14(8):497.
28. Ortiz MA, Mikhailova T, LI X. Src family kinases, adaptor proteins and the actin cytoskeleton in epithelial-to-mesenchymal transition[J]. Cell Communication Signaling: CCS. 2021;19(1):67.
29. Lin CW, Yang WE, Su CW. IGF2BP2 promotes cell invasion and epithelial-mesenchymal transition through Src-mediated upregulation of EREG in oral cancer[J]. Int J Biol Sci. 2024;20(3):818–30.
30. Newton K, Strasser A, Kayagaki N. Et Al Cell death[J] Cell. 2024;187(2):235–56.
31. CHUNG JK. Sodium iodide symporter: its role in nuclear medicine[J]. J Nuclear Medicine: Official Publication Soc Nuclear Med. 2002;43(9):1188–200.
32. Rakhsh-Khorshid H, Samimi H, Torabi S. Network analysis reveals essential proteins that regulate sodium-iodide symporter expression in anaplastic thyroid carcinoma[J]. Sci Rep. 2020;10(1):21440.
33. Nogales C, Mamdouh ZM, List M. Network pharmacology: curing causal mechanisms instead of treating symptoms[J]. Trends Pharmacol Sci. 2022;43(2):136–50.
34. Yu JSL, Cui W. Proliferation, survival and metabolism: the role of PI3K/AKT/mTOR signalling in pluripotency and cell fate determination[J]. Development. 2016;143(17):3050–60.
35. He Y, Sun MM, Zhang GG. Targeting PI3K/Akt signal transduction for cancer therapy[J]. Signal Transduct Target Therapy. 2021;6(1):425.
36. Izdebska M, Zielińska W, HAŁAS-WIŚNIEWSKA, M. Involvement of actin and actin-Binding proteins in Carcinogenesis[J]. Cells. 2020;9(10):2245.
37. Kumari R, Ven K, Chastney M. Focal adhesions contain three specialized actin nanoscale layers[J]. Nat Commun. 2024;15(1):2547.
38. Paggi JM, Pandit A, Dror RO. The Art and science of molecular Docking[J]. Annu Rev Biochem. 2024;93(1):389–410.
39. Paladino L, Vitale AM, Santonocito R. Molecular chaperones and thyroid Cancer[J]. Int J Mol Sci. 2021;22(8):4196.
40. Caner A, Asik E, Ozpolat B. SRC signaling in Cancer and tumor Microenvironment[J]. Adv Exp Med Biol. 2021;1270:57–71.
41. Eskandari E, Eaves CJ. Paradoxical roles of caspase-3 in regulating cell survival, proliferation, and tumorigenesis[J]. J Cell Biol. 2022;221(6):e202201159.
42. Gao J, Xiong A, Liu J. PANoptosis: bridging apoptosis, pyroptosis, and necroptosis in cancer progression and treatment[J]. Cancer Gene Ther. 2024;31(7):970–83.
43. Fresno Vara JA, Casado E, De Castro J. PI3K/Akt signalling pathway and cancer[J]. Cancer Treat Rev. 2004;30(2):193–204.
44. Song M, Bode AM, Dong Z. AKT as a therapeutic target for Cancer[J]. Cancer Res. 2019;79(6):1019–31.

45. Khezri MR, Hsueh HY, Mohammadipanah S. The interplay between the PI3K/AKT pathway and circadian clock in physiologic and cancer-related pathologic conditions[J]. Cell Prolif. 2024;57(7):e13608.
46. Karmokar PF, Moniri NH. Free-fatty acid receptor-1 (FFA1/GPR40) promotes papillary RCC proliferation and tumor growth via Src/PI3K/AKT/NF-κB but suppresses migration by Inhibition of EGFR, ERK1/2, STAT3 and EMT[J]. Cancer Cell Int. 2023;23(1):126.
47. Simón L, Torres K, Contreras P. et.al. Inhibition of Glycolysis and Src/Akt signaling reduces Caveolin-1-enhanced metastasis[J]. Volume 176. Biomedicine & Pharmacotherapy = Biomedecine & Pharmacotherapie; 2024. p. 116841.
48. Li Y, Dong M, Qin H. Mulberrin suppresses gastric cancer progression and enhances chemosensitivity to oxaliplatin through HSP90AA1/PI3K/AKT axis[J]. Phytomedicine: Int J Phytotherapy Phytopharmacology. 2025;139:156441.
49. Xiao X, Wang W, Li Y. HSP90AA1-mediated autophagy promotes drug resistance in osteosarcoma[J]. J Experimental Clin cancer Research: CR. 2018;37(1):201.
50. Oh JM, Baek SH, Gangadaran P. A novel tyrosine kinase inhibitor can augment radioactive iodine uptake through endogenous sodium/iodide symporter expression in anaplastic thyroid cancer[J]. Thyroid: Official J Am Thyroid Association. 2020;30(4):501–18.
51. Mortensen ACL, Berglund H, Hariri M. Combination therapy of tyrosine kinase inhibitor Sorafenib with the HSP90 inhibitor onalespib as a novel treatment regimen for thyroid cancer[J]. Sci Rep. 2023;13(1):16844.
52. Hashida S, Yamamoto H, Shien K. Hsp90 inhibitor NVP-AUY922 enhances the radiation sensitivity of lung cancer cell lines with acquired resistance to EGFR-tyrosine kinase inhibitors[J]. Oncol Rep. 2015;33(3):1499–504.
53. Johnson ML, Yu HA, Hart EM. Phase I/II study of HSP90 inhibitor AUY922 and erlotinib for EGFR-Mutant lung Cancer with acquired resistance to epidermal growth factor receptor tyrosine kinase inhibitors[J]. J Clin Oncology: Official J Am Soc Clin Oncol. 2015;33(15):1666–73.

## Publisher's note